A HOT-WIRE ANEMOMETER FOR PARTICLE COUNTERS

by

Nicholas H. Terrell

A thesis

submitted in partial fulfillment

of the requirements for the degree of

Master of Science in Computer Engineering

Boise State University

May 2015

BOISE STATE UNIVERSITY GRADUATE COLLEGE

DEFENSE COMMITTEE AND FINAL READING APPROVALS

of the thesis submitted by

Nicholas H. Terrell

Thesis Title: A Hot-Wire Anemometer for Particle Counters

Date of Final Oral Examination: 15 December 2014

The following individuals read and discussed the thesis submitted by student Nicholas H. Terrell, and they evaluated their presentation and response to questions during the final oral examination. They found that the student passed the final oral examination.

Sin Ming Loo, Ph.D.   Chair, Supervisory Committee

John N. Chiasson, Ph.D.   Member, Supervisory Committee

Donald Plumlee, Ph.D.   Member, Supervisory Committee

The final reading approval of the thesis was granted by Sin Ming Loo, Ph.D., Chair of the Supervisory Committee. The thesis was approved for the Graduate College by John R. Pelton, Ph.D., Dean of the Graduate College.

ACKNOWLEDGEMENTS

ABSTRACT

A Hot-Wire Anemometer for Particle Counters

Nicholas H. Terrell

Master of Science in Computer Engineering

Portable real-time air quality monitoring is becoming a reality. While the data

quality of these devices may be questionable, they have shown to be promising. One such

device is the optical particle counter. The particle counter functions by having laminar

airflow with constant velocity traverse the path of a laser beam within an airflow channel.

This thesis presents the design and integration of a hot-wire anemometer into the flow

channel. The addition of an anemometer allows for real-time airflow velocity

measurements to be performed and adjusted. Data from the anemometer can also be used

to directly offset irregularities in particulate measurements during flow speeds outside the

corrective capabilities of the fan. Experimental results show that an integrated

anemometer is capable of correcting varying external disturbances and improving the

accuracy of particle counting measurements.

TABLE OF CONTENTS

LIST OF TABLES

LIST OF FIGURES

LIST OF ABBREVIATIONS

ADC	Analog-to-Digital Converter
ARM	Advanced RISC Machine
CFM	Cubic Feet per Minute
CPC	Condensation Particle Counter
DAC	Digital-to-Analog Converter
DC	Direct Current
DMM	Digital Multi-Meter
EMF	Electromotive Force
EPA	Environmental Protection Agency
FAA	Federal Aviation Administration
HSIL	Hartman System Integration Laboratory
I^2C	Inter-Integrated Circuit
ISR	Interrupt Service Routine
LAN	Local Area Network
MEMS	Microelectromechanical Systems
OPC	Optical Particle Counter
PCB	Printed Circuit Board
PI	Proportional-Integral
PID	Proportional-Integral-Derivative
PM	Particulate Matter
PMON	Personal Monitor
PPL	Particles per Liter
PWM	Pulse Width Modulation
RC	Resistor-Capacitor
RF	Radio Frequency
RISC	Reduced Instruction Set Computer
RPM	Rotations per Minute

SD	Secure Digital
SLA	Stereo Lithography
SNR	Signal-to-Noise Ratio
SPI	Serial Peripheral Interface
SPOS	Single Particle Optical Sensing
TCP/IP	Transmission Control Protocol/Internet Protocol
TEOM	Tapered Element Oscillating Microbalance
UART	Universal Asynchronous Receive/Transmit
USB	Universal Serial Bus
WHO	World Health Organization

CHAPTER 1: INTRODUCTION

In recent years, the public is finding that air quality plays a vital role in the health of those exposed [1-4]. Yet, real-time monitoring remains largely inaccessible to the vast majority of the public. In order to facilitate this growing need for environmental air quality data, portable sensing systems have seen an increase in research and development. Among many of the various sensors, airborne particulate measuring devices remain one of the more difficult to develop. Factors such as cost, cross sensitivities, and battery life all play very important roles in a portable system. One method to reduce cost and prolong battery life is to use an axial fan instead of a pump. However, maintaining constant airflow characteristics (e.g., velocity) with a fan can be complicated. In this research, a fan-based particle counter is augmented with a hot-wire anemometer. Airflow velocity can be detected and then be used to vary the fan's rotational speed. With this addition, particulate measurements, such as counts or sizes, can be more accurately determined with airflow measurements.

1.1 Optical Particle Counters

By the 1970s, the link between cardiopulmonary diseases and airborne pollutants in the form of particulate matter (PM) became generally acknowledged amongst scientists in the areas of health sciences. However, many arguments arose challenging the actual effects on human health based on particulate sizes and concentrations. Data had been very limited at that time, especially concerning $PM_{2.5}$ (sizes less than 2.5μm). As a

consequence, airborne particulate matter has become increasingly studied in recent years [3].

The findings of the research performed in the last decade have continuously shown a general negative impact on human health in regions with certain PM characteristics. For example, the World Health Organization (WHO) estimates that airborne $PM_{2.5}$ is the source for an estimated 500,000 premature deaths every year [2]. A 2004 study shows possible connections between inflammation, coagulation, and heart rhythms in healthy younger men exposed to ambient, in-car and roadside PM [4]. Even simple in-door dust is capable of ranging from millimeters to nanometers in size and has been shown to increase the risk for developing cardiovascular and lung diseases [1].

Unfortunately, understanding the nature of particulates can be difficult. Air pollution monitoring generally requires expensive equipment and facilities not available to the average consumer. Thus, knowing what events generate harmful particulates and how the surrounding environment is impacted is made a difficult task. As a result, the Environmental Protection Agency (EPA) has shown great interest in the development of low-cost, real-time air monitoring technologies [5].

The wide array of possible environments in which an individual can experience exposure makes data collection fairly difficult. Portability has become an essential characteristic in many particle counter designs, bringing with it new and various challenges. As a result, newer particle counters make use of photosensitive electronic components that detect light blocked or scattered by PM. These devices are typically referred to as optical particle counters (OPC) and can vary greatly in price, sensitivity,

and size. Figure 1 shows the basic concept of a scattering-based OPC. The laser rests on one side of the flow channel and emits a beam orthogonal to the particulate flow.
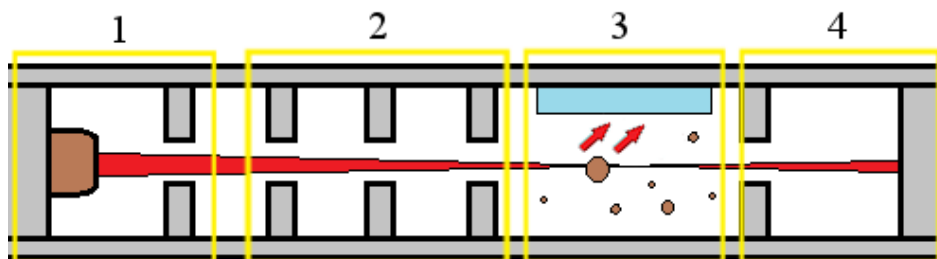
Figure 1: **Optical Particle Counting Cross-Sectional View; (1) Laser Source; (2) Light Blocks; (3) Particulate and Photodiode; (4) Laser Termination Point**

A series of light blocks protects the photodiode from errant light splashes potentially caused by the laser beam. The particulate, shown in (3) of Figure 1, crosses the beam and causes light to scatter towards the photodiode. The beam enters the termination point and is prevented from reflecting back into the flow channel. One should note that the particulate size and beam shape in Figure 1 are not to scale and have been exaggerated for clarity.

Portable OPCs require air sampling either through the use of a fan or a pump [6]. Pump-driven OPCs have the advantage of a consistent airflow velocity through the flow channel but are noisy and costly. Given that these devices are designed for use in many environments, noise pollution in home and workplaces may be deemed unacceptable.

A fan provides a more cost effective and quieter alternative to a pump. However, fans are not as consistent in performance. A fan's actual maximum rotations per minute (RPM) can vary greatly from unit to unit. There is RPM variation even for fans with similar part numbers. With only a fan available, there is no means of determining the actual airflow through the channel. Constant RPM can be achieved through a feedback control loop but does not confront the possibility of external disturbances (e.g., channel

blockages or external pressure variations) affecting the airflow. In order to track the actual airflow velocity in real-time, a sensor (such as a hot-wire anemometer) should be placed within the channel. The measurements can then be used to alter the fan's RPM set point to provide more or less airflow velocity. If the effects of airflow velocity on particle counts and measurements are characterized, then the results from the anemometer can also be used to enhance the overall accuracy of the particle counter.

1.2 Hot-Wire Anemometers

A hot-wire anemometer is a sensor capable of sampling subsonic or supersonic fluid flow velocities. Hot-wire anemometers generally consist of a micrometer thick wire, temperature control circuitry, and data acquisition circuitry. The wire can be installed inside a flow channel or a probe. The probe of the anemometer is then placed at the location where an airflow velocity measurement is desired. Probes are usually separated from the anemometer's heating circuitry and connected by leads. In some anemometer designs, the probe is part of small handheld rod as shown in Figure 2 and Figure 3. In other anemometers, the probe may only be an enclosure used to support the wire. The wire is made of a material that can withstand high temperatures without corroding.

By having airflow around the wire, convective heat transfer cools the wire, causing its resistance to drop. Based on calibration data and the temperature of the air, the resistance of the wire can be used to find the air's velocity. Hot-wire anemometers are generally limited to fluids with little conductivity (e.g., air) but have been used in other fluids such as liquid mercury [7].
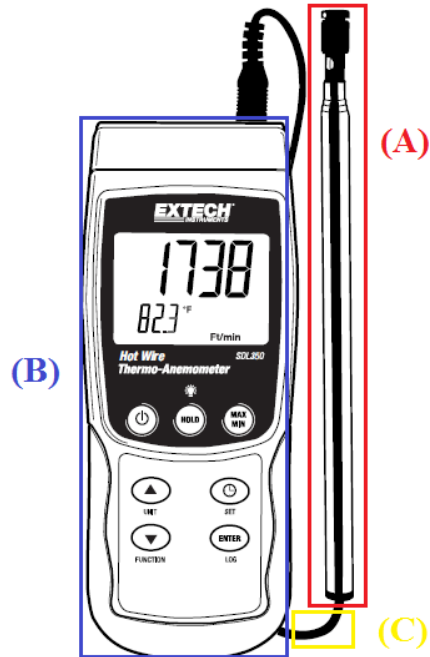
Figure 2: **EXTECH Instruments Hot-Wire Thermo Anemometer with Datalogger Model SDL350, where (A) is the Probe, (B) is the Datalogger and Heating Circuit, and (C) are the Probe Leads [8].**

Figure 3: **Zoomed View of EXTECH Probe**

1.3 Motivation

Particle counters must become portable and capable of operating in various

environments in order to supplement the growing need for PM data. If commercial

viability for the average consumer is desired, then the price of particle counters will need

to be lowered. OPCs can be made available in vehicles, homes, offices, and outdoor environments without an obtrusive presence. Ideally, little to no maintenance should be required to keep the OPC functional and accurate.

Wind gusts are common in the outdoors environment and can have drastic effects on airflow velocity and PM measurements. Portable OPCs are also expected to be on the move while collecting data. Movement velocities of high enough intensity can generate air resistance, changing the pressure levels around the inputs and outputs of the flow channel. By outfitting an OPC with a hot-wire anemometer, the OPC can become more robust towards these external pressure and air movement variations.

1.4 Contribution

While offering many advantages, a fan-driven OPC is an approach rarely demonstrated in past technologies due to the potential airflow consistency problems. The key contribution of this work confronts these problems by introducing the use of a hot-wire anemometer. The general approach is one to ensure limited negative impacts on the operation of the OPC and to bring a low-cost and maintainable sensor to the system. The impact of airflow changes on the reading of particulate concentrations is investigated. Accuracy of particulate counts is increased by compensating the counting algorithm with a known airflow velocity. The end result is a portable, multi-sensor system enhanced with an OPC more robust to various environments.

1.5 Work Overview

The work performed during this research is based upon previously completed portable sensor system designs. One of these designs has been named the Personal Monitoring (PMON) unit and was developed by the members of the Hartman System

Integration Lab (HSIL) at Boise State University. Contributions of this thesis to the PMON were based around the development of a new sensor system, the anemometer, in both hardware and firmware. Modifications to the PMON's existing firmware were also completed.

1.6 Outline

The rest of this thesis describes particle counters and hot-wire anemometers. Hardware and firmware implementation designs are discussed. Chapter 2 examines previous research in this area. Chapter 3 contains a brief overview for optical particle counting. Chapter 4 covers the theory behind hot-wire anemometry. Chapter 5 is where the hardware simulation, design, and results are discussed. In Chapter 6, a description of the firmware modifications and development applied is provided. Chapter 7 presents the results of the fully integrated system. This includes fan response and particle counting compensation. Chapter 8 concludes the thesis and offers potential areas for future work and improvements.

CHAPTER 2: PREVIOUS RESEARCH AND EXISTING TECHNOLOGY

This chapter discusses previous research and technology. It includes the design specifications on the base system used as the sensor platform. Existing technology, such as particle counters and hot-wire anemometers, is then presented.

2.1 Previous Research

As part of previous research, a portable particle counter had been developed for the mobile PMON platform (Figure 4). The PMON was developed by the HSIL for the Federal Aviation Administration (FAA) and was intended to evaluate air quality and detect contaminants within airliner cabins. A complete PMON is composed of the motherboard, the OPC, a feedback controlled fan, and various sensors.

Figure 4:   Full PMON Unit, Top Removed

2.1.1 PMON Motherboard

The PMON's motherboard is designed with flexibility in mind regarding sensor

integration, data management, and portability. It currently serves as a critical element in

the OPC, fully enclosing the topside of the channel. It comes equipped with Atmel's

AT32UC3A2 processor, which provides the control signals and analog-to-digital (ADC)

channels required to operate all sensors and the OPC.

Flat-flex cable (FFC) headers offer connection points for daughterboards designed

independently from the motherboard. These headers expand on the motherboard's

original functionality through communication protocols such as Inter-Integrated Circuit

(I^2C), Serial Peripheral Interface (SPI), Universal Synchronous Asynchronous Receiver

Transmitter (USART), and general purpose input output (GPIO). This makes the

platform flexible and versatile, allowing sensors to be swapped whenever necessary.

Besides communication protocols, direct current (DC) power is also provided to each

sensor through its respective FFC connection point. Several daughterboards are already

available from previous research and provided access to pressure, temperature, CO, and

CO_2 sensors for the PMON platform. Of these sensors, only temperature is required to aid

the anemometer in calculating the airflow velocity. The daughterboard containing the

thermistor was also used to fully enclose the flow channel. This allowed the thermistor to

be placed within the flow channel. The thermistor board is the only preexisting

daughterboard used in this research.

For the potential amount of data that could be generated in a portable multi-sensor

system, storage played a critical role. A micro Secure Digital (SD) slot is made available

on one of the sides of the motherboard and provides gigabytes worth of data storage. This

storage can be used for storing sensor measurements as well as system log files for potential run-time issues. An initialization file containing options, settings, and calibration information is also kept on the SD card. This allows certain system or sensor functionalities to be enabled or modified without the need for reprogramming. A mini Universal Serial Bus (USB) port could be used to access the SD card for added convenience.

Wireless communication, being fundamental for portability, is primarily accomplished through Zigbit protocols. This allows each PMON unit to operate as part of a mesh network, effectively extending the communication range between the data sources and delivery points. By changing options in the SD card initialization file, a PMON unit could be designated as either a coordinator node or a sensor node. Coordinator nodes act as end points to the data flow in the mesh network and usually interface with a database either via local area network (LAN) or Wi-Fi. The sensor nodes in the mesh network simply pass along information from one unit to the next until received by a coordinator. Bluetooth is also available on some units, and a real-time data feed can be accessed on Bluetooth-ready devices such as a smartphone or tablet. An Android application was also designed by HSIL for real-time plot generations on these devices.

Battery life is also another important consideration. In order to record data for a flight, the motherboard had to be capable of running at a very low power level. The initialization file on the SD card allows a user to turn off all unnecessary functions (e.g., Bluetooth, LED indicators, etc.) to conserve power. Certain sensors could be set to poll at lower sample rates to reduce power requirements as well. Power is supplied through six AA batteries. A barrel jack is also made accessible for the use of a 12V DC wall wart. A

two pin header is available on the underside of the motherboard so that a coin cell battery

could assist in maintaining the proper date and time for unpowered PMON units.

<u>2.1.2 Airflow Channel</u>

The airflow channel is a vital component to the particle counter system and is

designed to provide laminar airflow orthogonal to a laser beam. The PMON's channel is

10 mm deep by 6 mm wide and is approximately 50 mm long. The flow channel and the

PMON's enclosure are designed as a single component and cannot be separated (Figure

5).
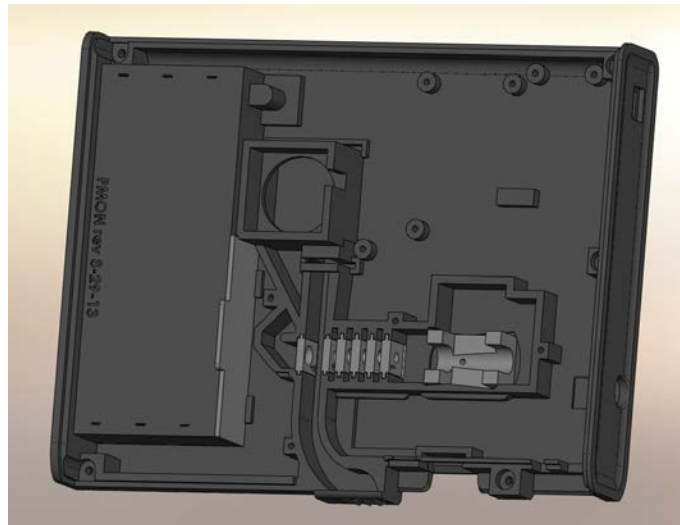
Figure 5:   **PMON OPC Flow Channel and Enclosure**

In order to prevent turbulence from being generated and introduced, the fan does

not force air into the channel directly. Instead, the fan is placed at the outlet and pulls the

air through the channel. A circuit senses electromotive force (EMF) pulses in the fan's

supply voltage, which then allows the processor to determine the rotational speed in RPM

(Figure 6). If a specific RPM is desired, the set point value can be set in the initialization

file on the SD card. Proportional-integral-derivative (PID) gain coefficients can also be

established in the file for proper control. Generally, the set point for the fan speed is

10,000 RPM, which is slightly under the fan's maximum performance capability. After

processing the error of the EMF pulse timing, the microcontroller updates the pulse-width

modulation (PWM) signal used to control the fan voltage.
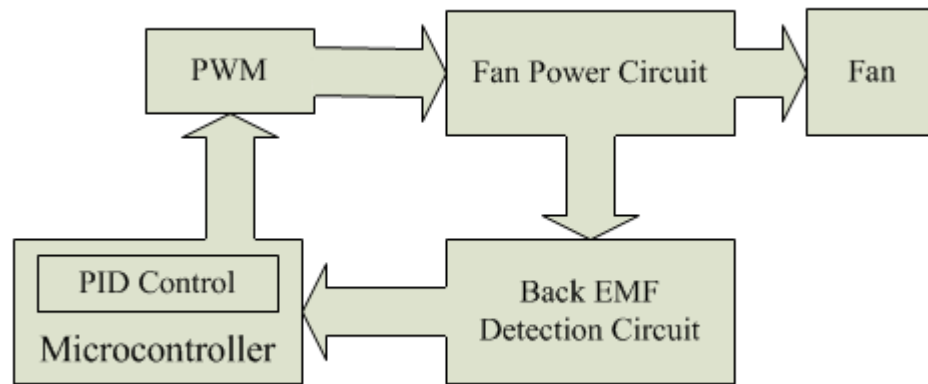
Figure 6: **Fan Control Block Diagram**

ANSYS computation fluid dynamics software was used to predict the behavior of

the air through the channel. While the airflow velocity is largely dependent on the

rotational speed of the fan, all simulations were performed with an airflow velocity of 4

m/s and showed stable laminar flow. SolidWorks enabled the 3D CAD design of the

channel, which could then be printed using stereolithography (SLA) technology.

The laser is installed in a turret capable of rotating around the axis normal to the

plane on which it rests. Once the laser is aligned, a screw can be tightened, locking the

turret in position. The beam is then emitted through a series of light blocks, which are

used to catch errant light splashes. A photodiode sensitive to the laser's frequency of light

rests in the flow channel and is fixed to the bottom side of the motherboard. The beam

passes under the photodiode and then terminates in a curved light trap. Any particulate

matter moving through the flow channel then refracts the beam's light, causing the

photodiode to receive pulses of varying durations and amplitudes.

Figure 7 demonstrates the airflow path relative to the incident laser beam. Air, signified as blue arrows, is pulled through the inlet and is then drawn through a curved path. The curved path is used to prevent external turbulences from having direct access to the flow passing under the photodiode. The red line represents the laser beam as it passes through the light blocks and crosses the flow channel. The point of intersection between the blue arrow and red length is the location of the photodiode.
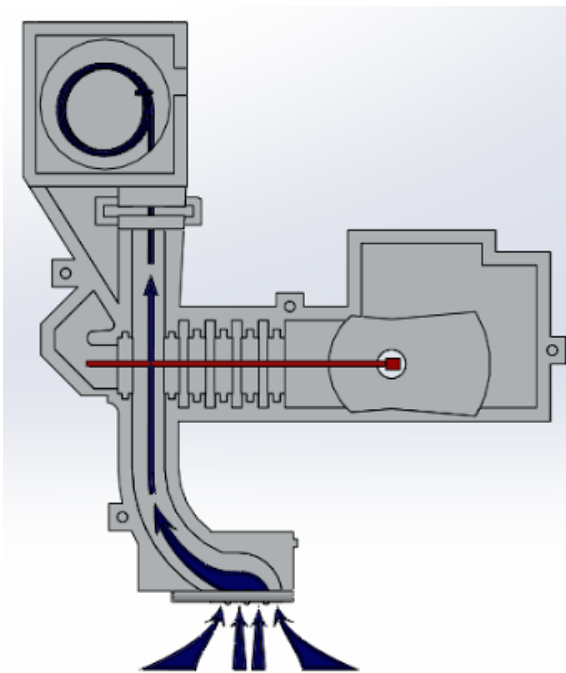
Figure 7:   PMON OPC Airflow Channel Showing Direction of Flow (Blue) and Incident Laser Beam (Red)

Since the analog circuitry of the particle counter must be placed relatively close to the photodiode, the top side of the flow channel is enclosed by the a circuit board. In this case, the circuit board is the motherboard. A tight seal between the motherboard and flow channel enclosure assembly must be maintained in order to prevent the airflow from being influenced by alternate input or output locations. Additionally, external light sources are capable of affecting the photodiode's measurements and must be limited to

the channel inlet and outlet locations only. To prevent light from reflecting into the flow channel, both the motherboard and the flow channel have matte black finishes.

2. 1. 3 Firmware and Software

The PMON's motherboard is set to run on a flexible codebase designed to easily select, enable, disable, and add sensors. Both low level and high level code is made to be modular, allowing quick changes between different platforms and setups. Each platform consists of a set of sensors appropriate for the intended research. A custom data manager routes the data flow going from each sensor source to the data log and wireless network.

While a database is made available, the data is more often viewed in real-time through a program called Sensor Monitor Lite, developed by HSIL. Sensor Monitor Lite allows the user to view all unit and sensor data from a designated serial port, Transmission Control Protocol/Internet Protocol (TCP/IP) address, or data log file. Previously acquired data can also be obtained from a database and then viewed in Sensor Monitor Lite. The graphing window allows for dynamic panning and zooming of captured data from one or more units. As an added feature, the data can be exported to a comma separated value (CSV) formatted file.

2.2 Existing Technology

2.2.1 Optical Particle Counters

Hall surmises that airborne particulate detection has been performed since people could see smoke from a fire [6]. Still, most particulate, especially that of $PM_{2.5}$, is invisible to the naked eye. Consequently, various particulate sensing technologies have been developed over time. These technologies vary considerably in design and functionality.

A device used in a study by the EPA consists of a technique that accumulates PM of various sizes on filters. At the end of a specified interval, each filter was removed and weighed to determine PM concentration levels. Impactors, cyclone heads, or specific filters could be used in order to capture particle sizes of interest [9]. While the device was capable of widespread use in many environments, its process required time for particle accumulation during which it could not be moved. Additionally, precise mass measurements had to be taken after a specified duration of exposure to the particulate. As a result, this device is not capable of obtaining real-time measurements nor can it be considered portable [10].

The tapered element oscillating microbalance (TEOM) is another approach that also uses the mass of the particulate to determine ambient concentrations. Instead of accumulating the PM on a filter, the TEOM collects PM on a glass element that oscillates due to an electric field. As more PM is caught on the element, the overall mass increases, thus changing the oscillation frequency. This allows for data to be collected in real-time. Still, the TEOM makes no improvements in the realm of portability as the device requires a considerable amount of setup time and cannot be moved during operation [10].

In an effort to increase portability, optical particle counting techniques have undergone much exploration. One of the earliest optical methods involved a light-obscuration approach also known as single particle optical sensing (SPOS). As described in [11, 12], fluid-borne particulate is traversed orthogonally to an incident laser beam. An extinction diode rests on the opposite side of the fluid and catches the beam after it passes through the fluid. Any shadowing caused by particulate results in the lowering of the

voltage generated at the extinction diode. The size and number of voltage dips can be used to determine particulate size and concentrations, respectively.

However, detecting the absence of light is much more difficult than detecting light itself due to diffuse reflectance. As a result, a light scattering approach is capable of higher sensitivities [12]. In a light scattering OPC, the photodiode is placed at an angle away from the incident laser. As particulate traverses through the laser beam, light is scattered in many different directions. The photodiode then captures some of the scattered light and generates voltage pulses. The pulse amplitude and duration is then used to determine the particle's size. The number of counts is scaled to determine the concentration in the ambient fluid. In comparison to the light obscuration method, the light scattering approach tends to be more costly due to the requirement of more sophisticated circuitry [11].

Some OPC designs combine both the scattering and obscuring techniques in order to cover a broader range of particulate sizes. For example, data from the laser extinction diode can be used to detect particulate sized 2.0 μm or greater whereas the scattering diode can be used to count particles of finer sizes [11]. This approach greatly increases the complexity of the classification system in firmware as well as the required circuitry.

Another common strategy is to grow condensation on the particulate being studied, as seen in condensation particle counters (CPC). Given that it can be incredibly difficult to detect particulate in the sub-micron range (<300 nm), particle size can be artificially grown with condensed alcohol. This increases the surface area of the particle and thus the amount of reflectance provided as it passes through the laser beam [13].

While extending the sensitivity range of OPCs, CPCs require additional apparatuses that make portability very difficult.

Of these optical methods, the single sensor scattering approach has been shown to be effective in producing smaller, less expensive particle counters. Dylos Corporation produces and sells single units for approximately $300 [14]. These units use a fan to drive the air through a flow channel. All data is collected through an attached screen or through a computer serial interface port (Figure 8). However, they do not contain any form of battery support and must remain connected to a power socket. They are also too large to be worn, being approximately 8 cm by 11 cm by 18 cm. As a result, these units are not portable. There is no particle size differentiation.

Figure 8:   Dylos DC1100 Air Quality Monitor [14]

TSI produces portable optical particle counters that are capable of differentiating between particles of several sizes. Unlike the Dylos units, the TSI Aerotrak devices do not use a fan to drive the air through the channel. Instead, a pump is used. While this may assist in the ability to accurately differentiate particle sizes and counts, the cost is

significantly higher. Depending on the desired model, each unit costs around $2000 to $4000.

2.2.2 Hot-Wire Anemometers

Hot-wire anemometers have arguably been in development since Boussinesq performed his studies on convective heat transfer with heated wires in 1905. A year later, King furthered Boussinesq's research and made pivotal progress by experimentally verifying heat transfer results from potential flow around a cylinder. From there, the first measurements of subsonic flows were obtained by Dryden and Kuethe in 1929 using what is now known as a constant current anemometer. Since then, various circuit types have been used to both heat the wire and keep one characteristic variable constant: current, voltage, or temperature [15, 16].

The simplest anemometer is the CCA, being the first created [16]. The CTA followed a few years after the CCA in design [15] and advanced its sensitivity and efficiency. The latest hot-wire anemometer type is the CVA, originally patented by Sarma in 1993 [17].

The hot-wire anemometer has been used primarily as an airflow velocity measurement tool in many areas of research. Air turbulence of jet flows have been thoroughly investigated using hot-wire anemometers [15, 18]. Air movement through the oro-pharyngeal-laryngeal parts of the human anatomy were studied in [19]. The airflow fluid dynamics of inkjet printers were studied using hot-wire anemometers in [20]. Sensor units were equipped with hot-wire anemometers and placed on aircraft in order to study air turbulence in atmospheric clouds [21]. The aerodynamics of insects during hovering flights was studied using anemometers in [22].

In addition to the measurement of airflow velocities, other uses for the hot-wire anemometer have been found and studied. In one instance, the anemometer was used as a particle velocity detector in standing sound waves [23]. Gas concentration measuring with an anemometer was shown to be viable for certain types of gases during mixing [24]. A hot-wire anemometer was also shown to be capable of capturing particulate counts in [25].

Using hot-wire anemometers in real-time control problems has already been shown to be viable by Huang in [18]. Placing micro-machined anemometers and control surfaces at the lip of a jet, a closed loop feedback control system could be used to assist in eliminating jet engine screech. However, the anemometers used were microelectromechanical systems (MEMS) and extremely small. MEMS-based anemometers are advantageous in that they are much more efficient and sensitive than standard hot-wire anemometer devices [18, 26]. However, they are relatively new and currently difficult to obtain for general public commercial applications at the time of this research.

CHAPTER 3: OPTICAL PARTICLE COUNTER

This chapter discusses the approach used for particle counting in this research. OPC design and calibration methods are presented. The impact of external airflow disturbances is briefly discussed. A detailed explanation on the effects of these disturbances can be found in Chapter 6.

3. 1 Overview of Optical Particle Counting

The OPC used for this research was designed by the HSIL at Boise State University. Based on the prices of commercially produced OPCs, particle counting has been fairly limited to high-end research or large-scale industrial applications. In order to consider the custom OPC to be successful, it was required to match the performance of these commercial devices. This proved to be a difficult task, as the commercial devices were not always in agreement amongst themselves due to their differing approaches in design and calibration [6].

3.1.1 OPC Design

Three variations of the OPC had been developed in the HSIL, although only one was used in the PMON system. The first OPC consisted of a single photodiode placed above the laser's incident area in the flow channel. The other two designs each contained a second photodiode, one placed in tandem and the other placed orthogonal to the original. These OPCs use the light scattering technique for capturing particulate data. This thesis uses the OPC version with a single photodiode.

Particles detected at the photodiode produces a very small current. A transimpedance amplifier is used to convert the photodiodes output current to a voltage. Two additional amplifiers are then used to scale the resulting voltage. The first amplifier provides a large amount of gain to facilitate the capture of weaker pulses caused by very small particles. The second amplifier's gain is set much lower so that larger particles would not saturate the ADC input and can be classified appropriately. While the actual size of each particle is difficult to determine in this setup, calibration methods can be employed to adjust the threshold between the small particle and large particle counts. By default, the small particle detection range is set between 0.3 µm and 1 µm. Anything larger than 1 µm was considered a large particle with a maximum detection limit of 25 µm.

3.1.2 OPC Calibration

Calibration remains a vital step in the development of each OPC. The accuracy of every particle counter is highly dependent on the reliability and consistency of the calibration methods employed. The calibration method described in [6] consists of using a gold-standard approach. A level of sensitivity consistently achievable between OPCs is set as the standard. Each OPC is then calibrated to that standard. Once calibrated, every PMON is checked against a commercially developed OPC to ensure proper counting accuracy. Two commercially available OPCs were used for two different particle count concentrations. For particle count ranges below 500,000 counts per cubic foot, the Particle Measuring Systems (PMS) Lasair II-110 [27] was used. Anything greater required the use of the TSI 9303 Aerotrak [28], which was capable of reaching a maximum of 2 million particles per cubic foot.

Each PMON unit undergoing calibration was placed into a chamber along with the Aerotrak handheld OPC. Pressurized air could then be fed into this chamber via one of four paths. The diagram in Figure 9 demonstrates the layout for this system and is also described in further detail in [6]. The first path was the flush line, which was a direct path from the source to the chamber. The air source was relatively clean and was capable of reaching concentration levels less than 1000 particles per liter (PPL). The next three paths all stemmed from the system feed route, which ran in parallel to the flush line. A collision nebulizer was placed in between all three routes and the system feed.

The first path coming from the nebulizer fed directly into the chamber, allowing cold particulate to remain intact. The second path ran through a heated pipe before allowing the particulate to enter the chamber. The last path contained desiccant to dry the particulate flowing into the chamber.

The cold and hot paths were used for greater particulate counts and required the nebulizer to be filled with a combination of tap water and de-ionized (DI) water. The impurities of the tap water were more than enough to generate counts in the millions per cubic foot. The DI water was used to dilute the tap in order to keep the generated particulate from saturating the chamber. The cold path could then be used to expose the units to a range between 200,000 and 600,000 counts while the hot path could extend the concentration range above 1 million counts. It should be noted that the particulate sizes varied but were kept relatively small.
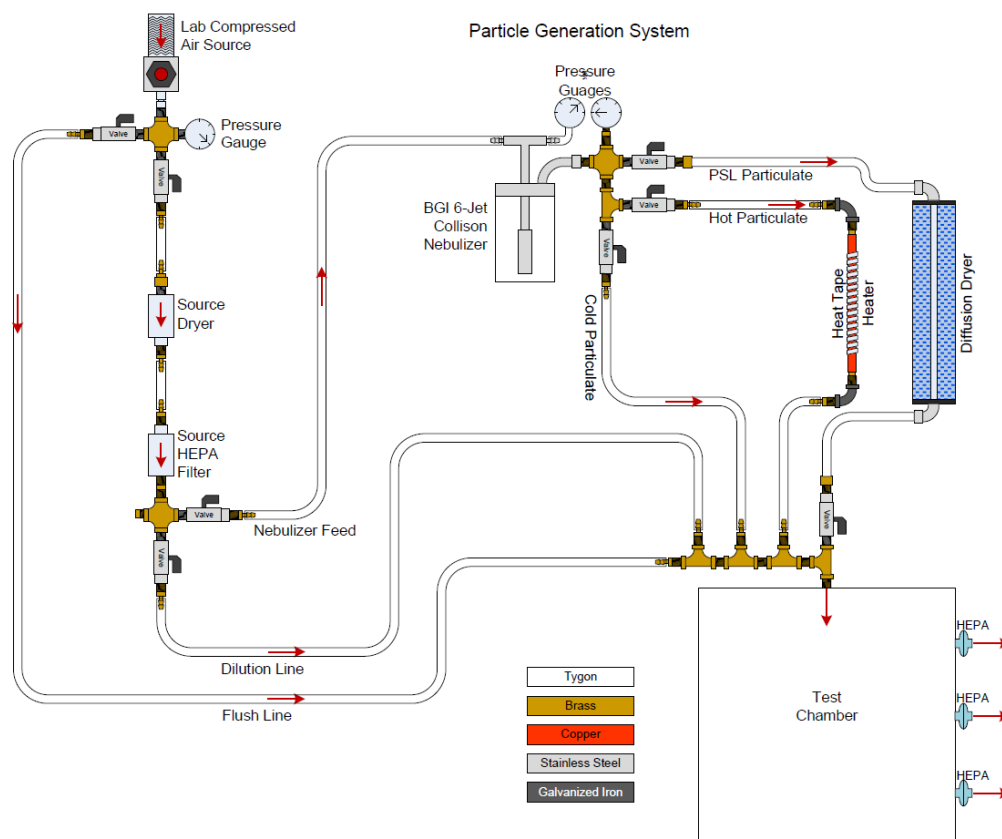
Figure 9:   Particle Generation System and Chamber Used for OPC Calibration [6]

The desiccant path provided a means of generating particulate of specific sizes and could also extend the obtainable particulate sizes. It did not require any tap water and instead used a mixture of polystyrene latex (PSL) and DI water in the collision nebulizer. The PSL, specifically designed for particle counter calibrations, was generally kept at sizes close to the threshold used to distinguish small and large counts: 0.6 μm, 0.8 μm, and 1.0 μm.

While the chamber successfully provided a means of consistent calibration concentrations, other important factors could vary internally within each PMON unit. These variances can greatly affect the scaling behavior of the particulate measurements and had to be addressed. As described in Section 3.1.1, OPC Design, every unit was

outfitted with a small laser module. These, being low cost laser modules, varied in beam shape and intensity. Each laser had to be characterized prior to calibration to ensure that it was capable of obtaining minimum levels of power output and that its shape would not drastically alter the ambient light levels in the airflow channel.

Another important factor was the airflow velocity through each unit's channel. Despite the simulations performed in ANSYS, the actual airflow velocity was never experimentally investigated in [6]. Hypothetically, a higher airflow velocity could potentially increase the number of particles flowing through the beam, leading to higher counts. At the same time, the increased velocity would also decrease the amount of time the particle spent in the laser beam. Both the higher counts and pulse changes could drastically alter the particulate measurements. Therefore, it was important to ensure each fan operated at the same RPM. Unfortunately, even if each fan was run at maximum power, discrepancies in the range of 1000 RPM would appear. This was a problem even for fans of the same model and manufacturer.

The original solution devised was to place a feedback control loop into the fan's power line [6]. Using the back EMF from the fan's magnetic pole pairs, each rotation of the fan could be tracked. The firmware for the particle counter would then count the number of rotations over a certain interval of time in order to determine the actual RPM. The feedback control loop could then use PWM to change the amount of voltage applied to the fan until a balance was found.

Unfortunately, this approach was unable to account for external disturbances. If large pressure variations were present at the inlet or outlet of a channel, the particulate

concentration measurements may have been greatly affected. This idea was first explored

by placing a 12 V fan with a static RPM orthogonal to the OPC intakes.
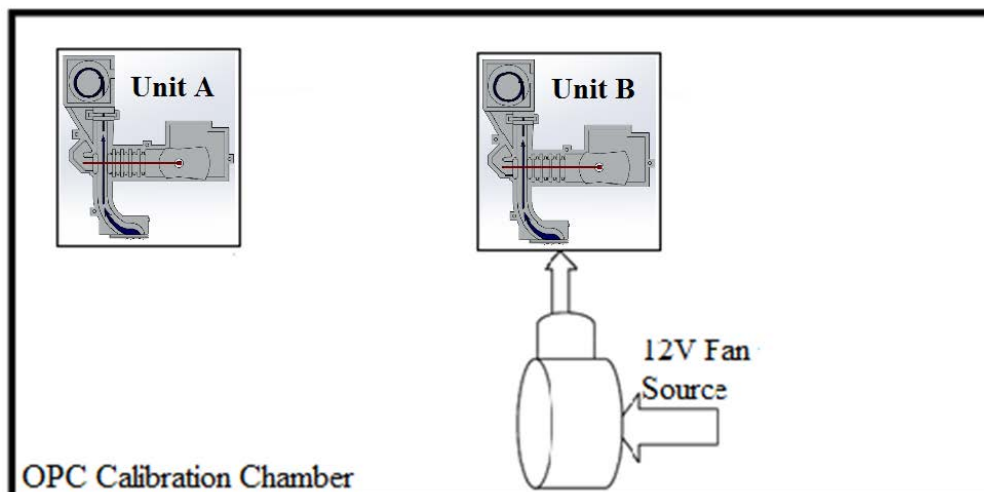
Figure 10:   External Airflow Disturbance Test in OPC Calibration Chamber

Two OPC units were also placed in the chamber with each having its particulate

measurements recorded. The external fan was placed facing the intake of Unit B as

shown in Figure 10. The second unit, Unit A, was placed on the other side of the external

fan, away from its intake. With the external fan in the off position, it was expected to see

a slow decline in the particulate count as the air inside was slowly exchanged with

filtered air. Opening the door to the chamber provided enough ambient PM in order to

observe this trend, which did occur as expected. However, when the fan was placed in the

on position, the trend was momentarily disrupted by an offset count as shown in Figure

11.
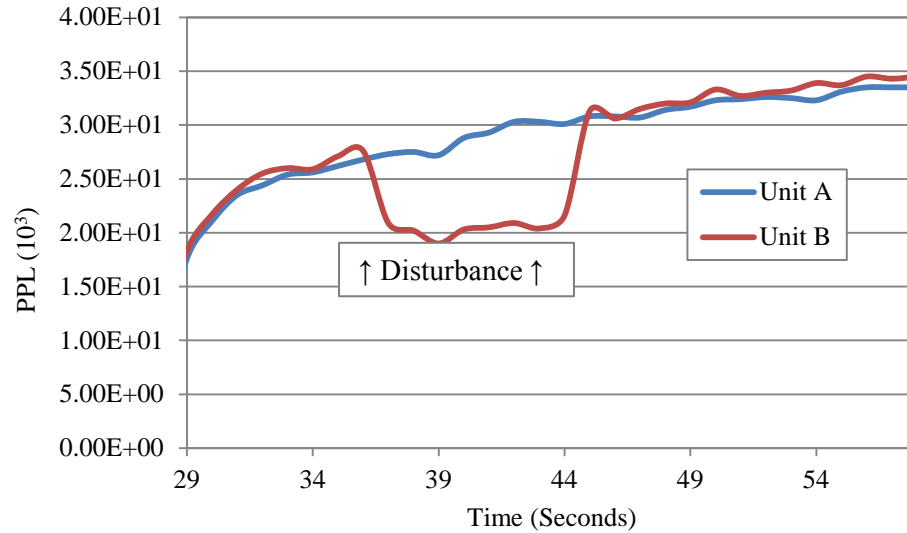
Figure 11:   External Airflow Disturbance Test Results

While it was originally expected that the PPL measurement of Unit B might increase due to more particles traveling through the laser beam, the assisted airflow actually resulted in a large decrease of its PPL measurements. This was potentially caused by a decrease of the pulse width or amplitude generated by each particle. Changing pulse characteristics could lead to missed trigger conditions or inaccurate particle classifications.

In order to understand what may be required to properly compensate for measurement inaccuracies, the effects that varying airflows have on the particle counter's hardware will need to be explored. This is discussed further in Section 6.1.2, Effects of Varying Airflow on Particle Counts.

CHAPTER 4: HOT-WIRE ANEMOMETER

The contents of this chapter are centered on the physical equations used by the hot-wire anemometer. By exploring the relationships between convective heat transfer, fluid dynamics, and resistance equations, expected behavior of the anemometer can be predicted.

4.1 Theory

Convective heat transfer plays a direct role in the calculation of fluid velocities. This is accomplished by heating a thin wire to a known temperature and then passing a fluid of a known temperature around the wire. The change in the wire's temperature is indicative of the fluid's velocity. Physical equations are required to determine the temperature of the wire and the heat transfer coefficient used in the end calculation [15, 16, 24].

The first equation is that of the relationship between the wire's resistance and its temperature,

$$R_w = R_0[1 + \alpha(T_w - T_0)]. \tag{1}$$

where R_w is the new resistance of the wire, R_0 is the resistance at the time of calibration, T_w is the current temperature of the wire, T_0 is the temperature of the wire at time of calibration, and α is the temperature coefficient of resistance belonging to the wire's material. Platinum, tungsten, or a combination of the two elements is usually selected due to their resilience against corrosion. Based on pricing and availability, tungsten wire was

selected for this research. Tungsten's temperature coefficient is $4.5 \times 10^{-3} \ (C°)^{-1}$. Since the present resistance of the wire is more easily found than the temperature of the wire, Equation (1) is rearranged for T_w, or

$$T_w = \frac{1}{\alpha}\left(\frac{R_w}{R_0} - 1\right) + T_0. \qquad (2)$$

At this point, both the resistance of the wire and the temperature of the wire should be known. If either the current through the wire or the voltage across the wire is also known, then the power into the wire can be determined. The power dissipated at the wire is used to increase its temperature, which is then affected by several types of heat transfer: radiation, conduction, and convection. If the majority of the heat transfer is performed through convection, then both radiation and conduction can be assumed to be negligible, leading to Equation (3),

$$P_w = hA_w\left(T_w - T_f\right). \qquad (3)$$

where P_w is the power dissipated at the wire, h is the heat transfer coefficient, A_w is the cross section area of the wire, and T_f is the temperature of the fluid. This follows the assumption that all power dissipated at the wire is accomplished through convection. Unfortunately, this assumption may not always be accurate. If the temperature of the wire exceeds a certain level, radiation heat transfer will begin to dominate the net energy loss in the system. The end result is a decrease in convective sensitivity and wasted power.

The heat transfer coefficient is a function of the airflow velocity; it provides the necessary connection between the airflow physical equations and circuit equations. This is accomplished through the Nusselt number. The Nusselt number (Nu) is a dimensionless value that represents the temperature gradient at the surface of a heated object [29]. While the form of the equation representing the Nusselt number varies based

on the geometry of the surface, it is always dependent on the Reynolds number (Re), and the Prandtl number (Pr). For a wire, Kramers experimentally demonstrated [30] that

$$Nu = A\, Pr^p + B\, Pr^q Re^n, \tag{4}$$

where A, B, q, p, and n are constants discovered at time of calibration. The Reynolds number, a ratio between inertial and viscous forces, is defined as

$$Re = \frac{U d_w}{\nu}. \tag{5}$$

In Equation (5), the Reynolds number is composed of the fluid velocity U, wire diameter d_w, and the kinematic viscosity ν. The Prandtl number, a ratio between viscous and thermal diffusion rates, is based on the temperature and type of fluid, which, in this case, is air. The identity for the Nusselt number offers the final connection point between all the expressions:

$$Nu = \frac{h d_w}{k}. \tag{6}$$

In Equation (6), h is the heat transfer coefficient, d_w is the diameter of the wire, and k is the thermal conductivity of the fluid. Substituting Equations (5) and (6) into Equation (4) yields

$$\frac{h d_w}{k} \ Nu = A\, Pr^p + B\, Pr^q \left(\frac{U d_w}{\nu}\right)^n. \tag{7}$$

Since d_w and k are both constants, they can be rearranged on the other side of the equation and absorbed by A and B, leaving

$$h = A\, Pr^p + B\, Pr^q \left(\frac{U}{\nu}\right)^n. \tag{8}$$

If the temperature of the fluid remains constant, then the values of ν and Pr will also remain constant once the sensor is calibrated. However, in this research, the

temperature may be varied and will be measured by a thermistor for proper

compensation. Rearranging Equation (3) and substituting into Equation (8) reveals that

$$\frac{P_w}{A_w(T_w - T_f)} = A\,Pr^p + B\,Pr^q\left(\frac{U}{\nu}\right)^n. \tag{9}$$

Finally, Equation (9) can be modified to come to the final expression for fluid

velocity:

$$U = \left[\frac{D_w P}{kA_w BPr^q\left(\frac{D_w}{\nu}\right)^n(T_w - T_f)} - \frac{A\,Pr^p}{BPr^q\left(\frac{D_w}{\nu}\right)^n}\right]^{\frac{1}{n}}. \tag{10}$$

As can be seen in Equation (10), calculating the airflow velocity can become

fairly computationally intensive, especially for a processor that has to deal with other

tasks. This equation will need to be simplified to make it viable for a microcontroller.

Further discussion on the simplification, approximation, and application techniques of

this equation can be found in Section 6.2.4, Anemometer Calibration.

4.2 Constant Current Anemometer (CCA)

As signified in its name, the CCA contains a constant current source, which is

used to heat the wire. The wire rests in one leg of a Wheatstone bridge, whereas the other

leg of the bridge is used to generate a reference voltage (Figure 12). The difference

between the two legs of the bridge is then amplified and captured by data acquisition

circuitry. A compensator can be used to adjust the gain applied based on the switching

frequency of the signal.
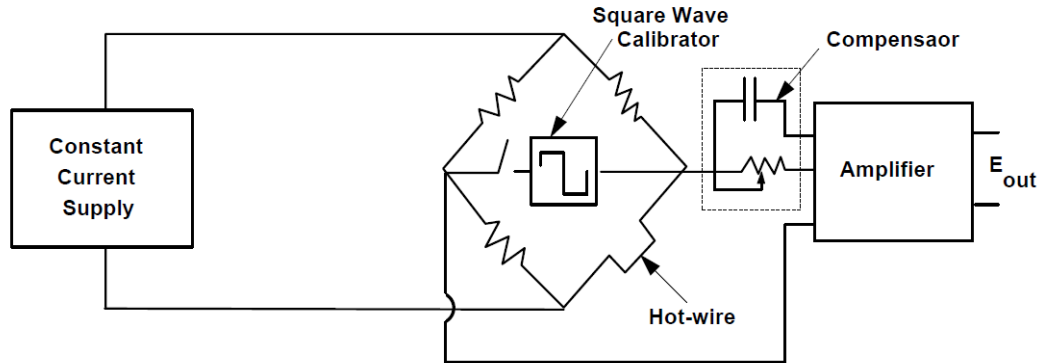
Figure 12:   CCA Circuit [15]

The CCA's simplicity is its strongest advantage. Component costs are generally lower than those required for the CTA and CVA. Computing results from a CCA is straightforward, requiring little processor time. Operating regions can be easily selected by choosing different resistor values for the bridge, and no stability problems will occur since the system remains open loop. Unfortunately, the constant current leads to a lack of sensitivity, especially at high frequency velocity changes. This is due to the continuous heating of the wire. Extended heating periods without airflow will result in temperatures higher than what is desirable. Radiation and conductive heat transfers will prevent the wire's temperature from increasing indefinitely, but will also lead to wasted power.

The CCA remains the least effective approach when attempting to accurately capture data in sensitive applications since amplitude responses diminish as airflow velocity fluctuations increase in frequency. This is due to the time constant limitations of the wire, as even extremely thin wires require time to reach proper temperature levels. One approach used to aid in increasing sensitivity is to increase the gain of the amplifier as the frequency of the fluctuations increases. However, this still is limited by any noise present in the system. A maximum frequency is obtained when the signal-to-noise ratio (SNR) value present post amplification has fallen below desirable levels.

4.3 Constant Temperature Anemometer (CTA)

Instead of using a constant current supply, the CTA (Figure 13) contains a variable current supply that is controlled by an analog feedback loop. Just as in the CCA, a Wheatstone bridge is used to apply a voltage across the wire and to produce a reference voltage. The error between the wire voltage and the reference voltage is then amplified and used to increase or decrease the current delivered from the supply. The current is also captured as airflow velocity data.
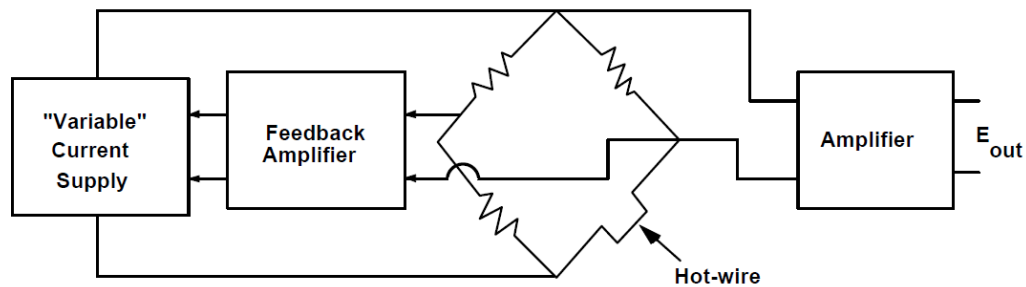
Figure 13:   CTA Circuit [15]

The result is that the temperature and resistance of the wire is maintained whether or not fluid fluctuations exist. This leads to the obvious advantage that no power is wasted overheating the wire. A second advantage is that the temperature of the wire does not change. Ideally, the amount of current being drawn should be almost identical in every instance where the airflow velocity is the same. In other words, the time constant for heating the wire is removed from operation once the wire has been initially heated. This allows the CTA to operate at frequencies much higher than that of the CCA.

These advantages remain intact for airflow velocities that do not stray too far from an average. The bandwidth of the CTA does not always remain constant for any given velocity range without having been calibrated or constructed for that specific range.

Some methods have been employed to counteract this disadvantage, such as adding a second feedback loop capable of altering the parameters of the initial feedback loop as described by Ligęza in [31]. Another disadvantage is that the CTA's response is limited by the amplifier's response time in increasing the current flow. Airflow fluctuations that occur at a frequency outside the operation amplifier's functional bandwidth cannot be properly compensated and will not appear in the data acquired. Probe lead length also places a role in the performance of the anemometer. Long leads are susceptible to radio frequency (RF) noise, which can also be a problem inherent to the CCA. This RF noise can be a significant problem if large gains are applied to make up for small temperature differences between the wire's operating temperature and the ambient temperature. The system is closed loop and can fall into instability if the Wheatstone bridge is not properly balanced.

4.4 Constant Voltage Anemometer (CVA)

The CVA (Figure 14) accomplishes its constant voltage by placing the wire in a T-resistor network of an amplifier's feedback loop, removing the bridge that was seen in the CCA and CTA. Even if the wire's resistance changes, the voltage remains constant, thus allowing the current through it to be read as airflow velocity data.

By holding the voltage across the wire and probe leads constant, RF noise and lead capacitance are no longer problems. The SNR becomes much higher, allowing greater amplification to be used, eliminating the need for high overheat temperatures. The time constant of the wire becomes present again but is reduced due to lower overheating. Balancing bridge resistances is no longer required in the CVA.

With the return of the time constant to the system's operation, bandwidth issues can be a problem for higher frequencies. The CVA's bandwidth is immediately greater than the CCA's bandwidth, but should be improved by certain techniques such as placing a resistor-capacitor (RC) network in the feedback loop of the amplifier. An additional composite amplifier can be placed on the output of the primary amplifier to further enhance the bandwidth [17]. While probe lead lengths do not contain capacitance problems, they do contain resistances that have been shown to increase thermal lag, decreasing accuracy. The lead resistance should be measured prior to operation in order to predict the effects of the additional thermal lag [32].
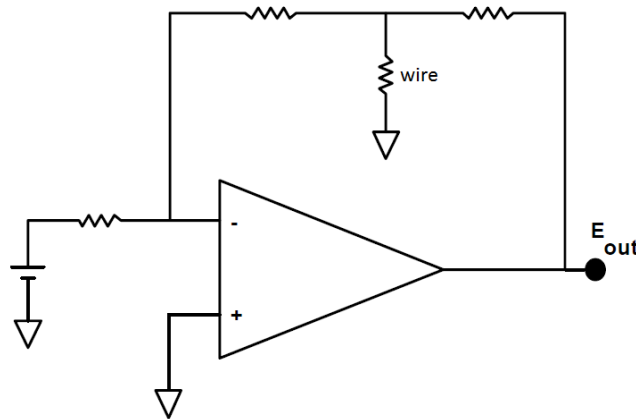
Figure 14:   CVA Circuit [15]

CHAPTER 5: HARDWARE DESIGN

This chapter presents the design and hardware implementation of CCA, CTA, and the anemometer probe. The components were selected based on results of simulations. Analysis of each implementation is also shown in this chapter.

5.1 Anemometer Probe

As described in Section 1.2, the anemometer probe is the sensing point of a hot-wire anemometer. It is composed of the wire and a supporting structure. The structure is used to hold the wire taut and to direct the airflow around the wire. It also provides an interface between the wire and the leads connected to the heating circuit.

5.1.1 Wire Resistance Estimation

The starting resistance of the wire is affected by its material type and geometry, as described by

$$R_w = \frac{\rho L_w}{A_{xw}},$$ (11)

where R_w is the wire resistance, ρ is the wire resistivity, L_w is the wire length, and A_{xw} is the cross-section area of the wire. Since 12 μm thick tungsten wire was selected for use in this project, ρ was 5.6×10^{-8} Ωm and A_{xw} was 1.131×10^{-10} m^2. Effectively, the resistance of the wire was related to its length by a factor of almost 500. Given that the current flow channel design is 6 mm in width, the resistance of the wire should be approximately 3Ω. Since the length of the wire will exceed the width of the channel and

the leads into the probe will contain resistance, the actual starting value for R_w is estimated to be slightly higher.

The maximum value of R_w was dependent on the type of anemometer and its circuit's bridge resistor values. If the ratio between balanced legs was $1:10$, then the top resistance of the probe leg needs to be 10% of the value of the top resistor of the reference leg. As the resistance of the wire increased, the wire voltage increased, which caused the bridge difference to go to zero. If the voltage across the wire surpassed the voltage across the lower resistor on the reference leg, then the output of the bridge would become negative. Negative voltages require more power regulation and signals to manage making data acquisition unnecessarily difficult. Therefore, they were avoided by making the lower resistor of the reference leg a value high enough to prevent this from occurring.

The balancing of the bridge legs leads to the implication that the bottom reference resistor can be used to control the operating temperatures for both the CCA and CTA. For example, if the resistance of the probe was 3.3Ω, then the lower reference resistor could be 36Ω. Using Equation (2), Figure 15 was generated. With the assumption that calibration occurred at room temperature, the temperature of the wire could then be estimated to be $316K$ (given a balanced bridge voltage). One important note is that instabilities may occur if the bridge voltage goes to zero or negative during a CTA's operation.
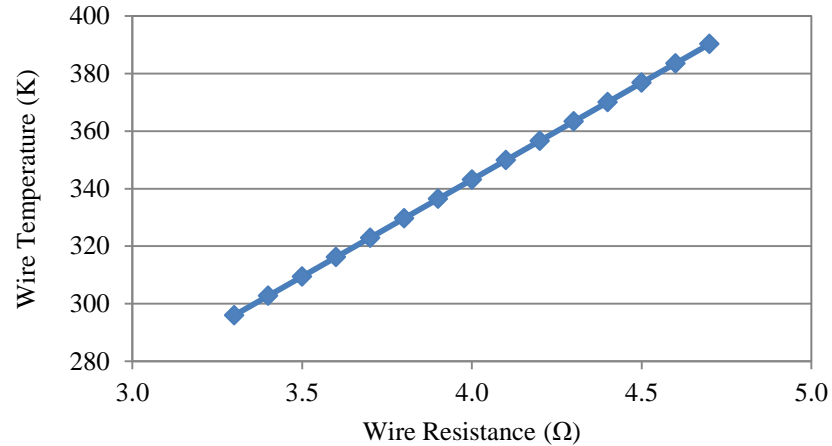
Figure 15: **Estimation of Temperature for Resistances of Tungsten Wire**

5.1.2 Probe Design and Implementation

Two probe types, one for the existing OPC flow channel (Figure 16a) and another

for the test channel (Figure 16b), were created. The length of each probe wire was

dictated by the width of each flow channel. Since the test channel's width was 3 mm, the

effective length of the wire was also 3 mm. Following the same convention, the probe

wire for the OPC had an effective length of 6 mm. The differing wire lengths between

each channel type led to differing resistances for each probe. The thickness of the white

wires in Figure 16 has been exaggerated for clarity.
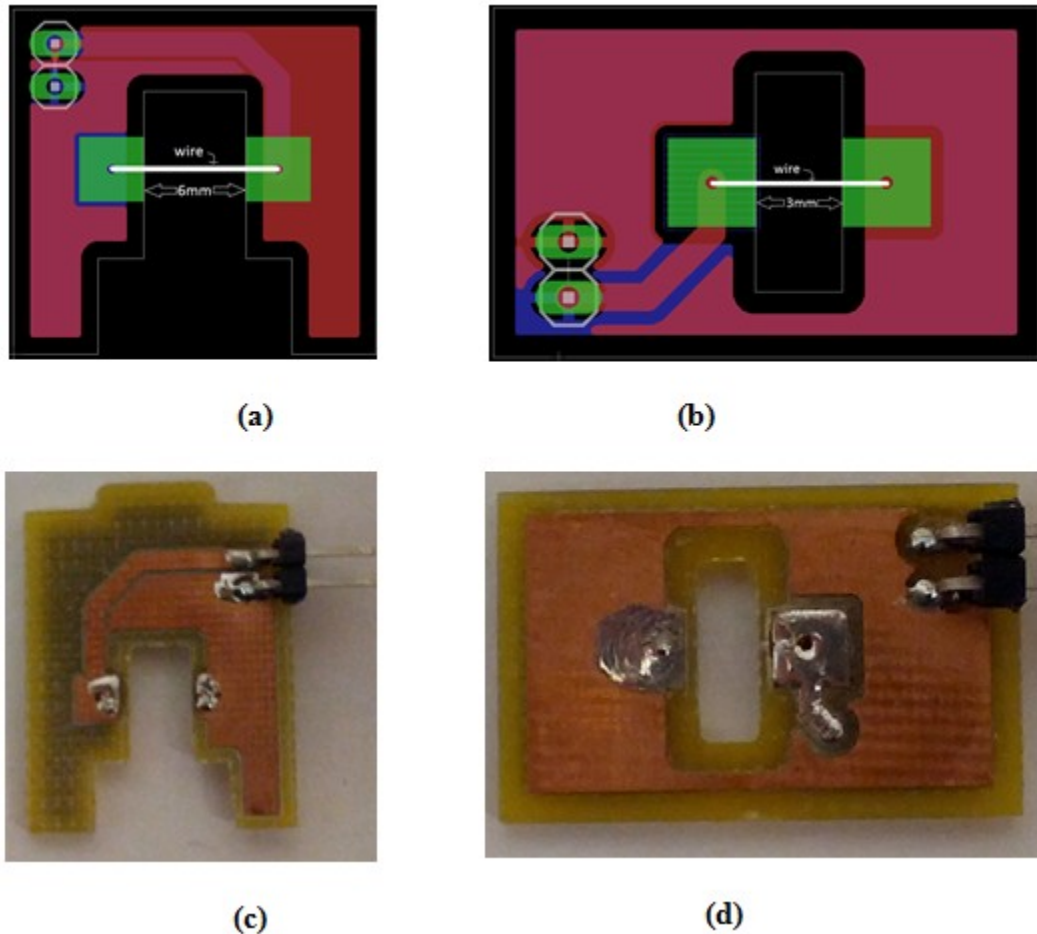
Figure 16: **(a) Probe Layout for the OPC Flow Channel, (b) Probe Layout for the Test Channel, (c) Actual OPC Probe, (d) Actual Test Probe**

Both probes were two layer PCBs with copper pads containing 0.6 mm holes positioned on opposite sides of a rectangular cutout. Unlike the test channel's probe, the OPC's probe had a cutout that was not fully enclosed since the prototype enclosure dimensions would not permit a groove extending into the floor of the channel. The size of the probe was made to be only as large as structural stability required. A two-pin right angled header extended off the side, each pin giving access to one end of the wire.

The implementation process consisted of inserting the wire through both holes, pulling it taut, and then applying solder to each pad. In order to ensure a good connection at the joint, the solder needed to fully enclose the tungsten wire. Since the length of the

wire was effectively controlled by the locations of electrical contact, each probe needed to have its wire soldered in the exact same locations. Ideally, this location is as close to the cutout as possible such that the length of the wire is close to the actual width of the flow channel. Excess solder was consciously avoided as it made inserting the probe into the channel a much more difficult task.

Applying extreme amounts of heat to the wire may have resulted in damages. However, ensuring that the flow channel was fully enclosed around the wire required specifically shaped material that could be reproduced consistently. PCB proved to be the best solution at hand given the resources available.

Both PCBs were designed with a cutout approximately the same width as that of their respective flow channels. The test channel's cutout extended into the floor of the flow channel and the OPC's channel contained grooves on the sides. The test channel was designed to simply provide laminar flow for calibration purposes. No photodiode or laser was present in the system and the anemometer could be placed anywhere within the laminar region. The placement of the anemometer into the OPC channel, however, required laminar flow at a location downwind from the photodiode. This was required due to the possibility that the anemometer's wire could potentially disrupt the laminar flow if resonated at specific frequencies. Any turbulence in the channel could cause the OPC to misread particulate data.

The probe leads were simple copper wires with female connectors on both ends. Their length was kept as short as possible in order to reduce unnecessary capacitance and resistance. While the test channel did not require the use of probe leads, they were still

used in order to simulate proper behavior when running in the PMON platform. The

leads' combined resistance was approximately 0.145 Ω.

5.1.3 Results

After the assembly of a probe, its resistance was measured to ensure proper

connections were made between the wire and the solder joints. If the results varied too

often or an open circuit was found, the joints were re-soldered and new wire was applied.

It was commonly found that each smaller probe was around 2.4 Ω and each larger probe

was around 3.5Ω, as predicted in Section 5.1.1. While not entirely certain, the excess

resistance may have been a result of wire damage that may have occurred during the

soldering process. Applying excessive heats to the solder pad may have exposed the wire

to unnecessary temperatures for prolonged periods, causing the wire to expand. Cooling

the wire would cause it to contract and possible form breakages along its exterior. As a

precaution, the lowest soldering temperature available was applied to the pads.

The connection points for each wire end were placed as close to the edge of their

respective pads as possible. This assisted in achieving consistent wire lengths. Any

connections made further from the edge also resulted in an instant increase of the wire's

starting resistance. Ultimately, it took several creation iterations before usable probes

were produced.

5.2 Constant Current Anemometer

Due to its ease of implementation, a CCA was the first proof of concept

prototype. The design of each hot-wire anemometer type began with LTSpice

simulations. When compared to previous hot-wire anemometer applications, the rate of

change of the airflow velocity through the OPC flow channel is relatively low. Thus, it

was not necessary to include a large bandwidth in each circuit design. These prototypes

provided a platform around which the rest of the firmware could be developed.

5.2.1 CCA Simulation

Using LTSpice, the CCA circuit was simulated to determine operating

boundaries. A constant current source delivered 50 mA to the bridge, overheating the

wire and generating the reference voltage. The top resistors of the bridge, R_a and R_b,

were held to a proportion of 1:10, respectively (Figure 17). This meant that the bridge

would balance when R_w achieved a value equivalent to a tenth of the resistance of R_{ref}.

Since the value of R_w was dependent on the type of probe being used, two primary

operating points for R_{ref} were tested.
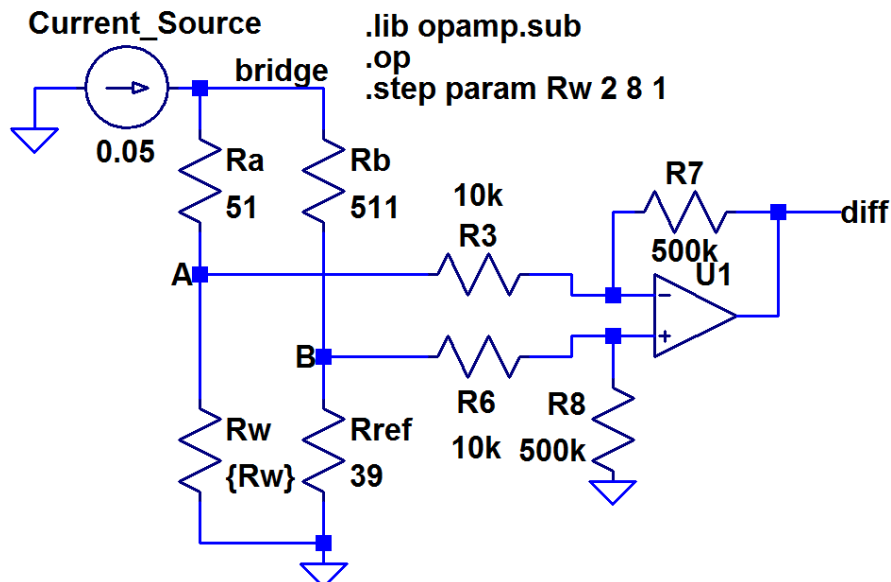
Figure 17:   LTSpice CCA Circuit Simulation

The probe with the 3 mm wire was simulated by stepping R_w from 2Ω to 4Ω in

increments of 0.1Ω. The value of R_{ref} was set to 39Ω, being the closest value available

for a resistor. This resulted in a peak voltage difference output of 80 mV when the

resistance was at its lowest point. As the motherboard does not supply negative voltage, the differential amplifier could only output zero volts. This occurred when the value of R_w exceeded a tenth of the value of R_{ref}. While 80 mV was easily within the input range of the ADC, it did not make good use of the ADC's 12-bit resolution. The differential amplifier stage was altered to provide a gain of 50 to the difference of the voltages. Applying this gain resulted in an output voltage range of 4V to 0V. While this placed the operation slightly outside the acceptable range of the ADC, the average minimum resistance of the 3 mm probe was 2.5Ω. Figure 18 shows that the voltage output for a 2.5Ω wire was 3V, which was within the ideal operating range.
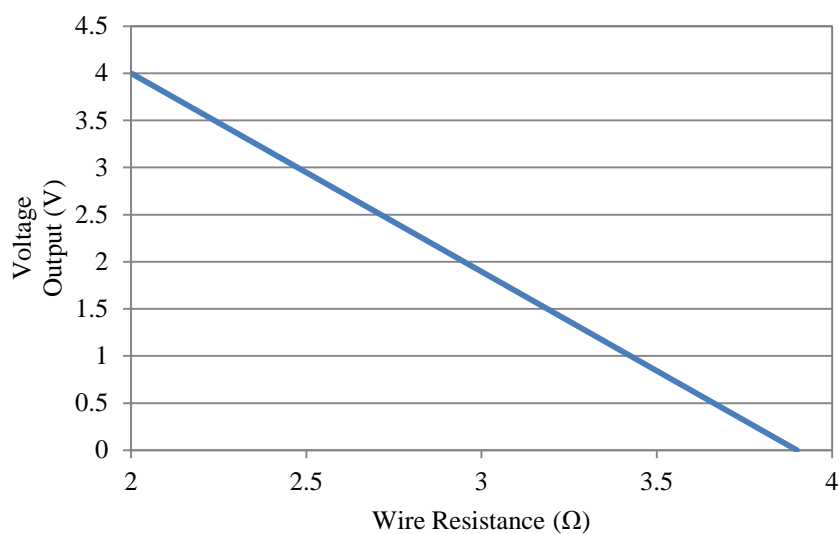
Figure 18:   LTSpice CCA Simulation Voltage Output over Wire Resistance

Applying a similar approach for the probe with the 6 mm wire, R_w was stepped from 3 to 5Ω in increments of 0.1Ω. This time, a 47 Ω resistor was set in place for R_{ref}. Similar to the results seen for the 3 mm probe simulation, the voltage output of the circuit varied from 3.6 to 0 V, being slightly over the operating range of the ADC. Once again, this was ignored due to the actual resistance of the probes being higher than 3Ω.

5.2.2 CCA Design

The anemometer circuit was placed on a two-layer PCB with a current source, Wheatstone bridge, differential amplifier, and an ADC. On the same board was also a thermistor circuit, which was used to detect the ambient temperature for the velocity calculations. All integrated circuits operated at $3.3\ V$ with the exception of the current source, which was powered at $5\ V$.

The constant current source aimed to provide approximately 50 mA to the bridge in order to generate the reference voltage and to heat the filament. By using a MAX1818 linear voltage regulator and placing a resistance between its output and ground (see Figure 19), a constant current could be generated for any load between the regulator's ground and the circuit's actual ground.

The constant current then was fed to the bridge where two voltage dividers created a reference and a wire voltage. The first leg, referred to as the probe leg, was composed of R9 and the probe. The second leg was labeled the reference leg and was composed of R1, R2, and R11. By using a trimpot as R11, the overheat level could be easily adjusted, compensating for any variation between probe resistances. The resistance of the probe was around 3.3 Ω at room temperature; having a 39Ω resistor mirroring on the reference leg forced the probe to overheat until it was about 3.9 Ω. This temperature was approximately $336\ K$.
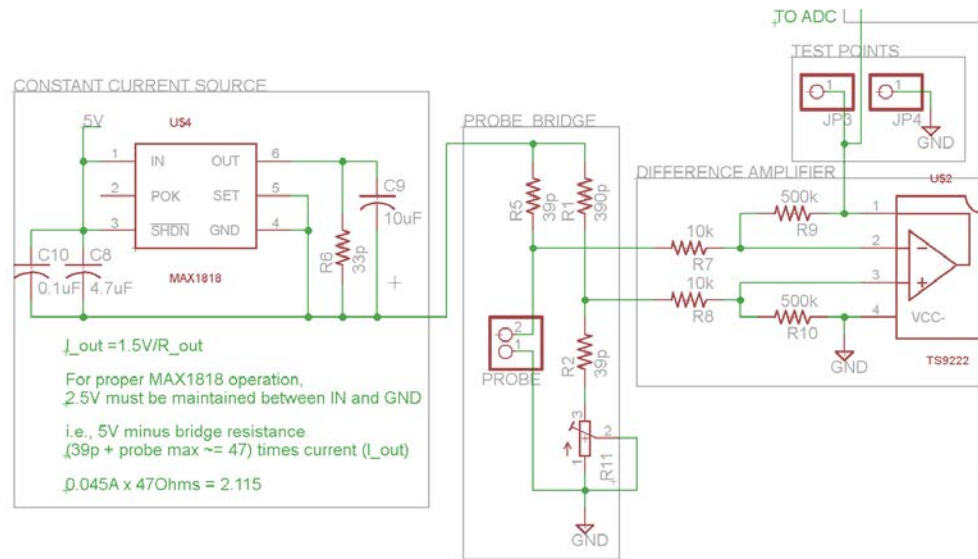
Figure 19:   CCA Eagle Schematic

The two voltage levels were then sent to a differential amplifier with the probe voltage fed into the negative input. The operational amplifier was powered by a 3.3V supply on its positive rail and grounded on its negative rail to prevent negative values from being propagated. After a gain of 50 was applied to the signal by the amplifier, the output could be read by a digital multi-meter (DMM) probe or through an ADC. For this project, ST Microelectronics' TS9222 was selected for the operational amplifier and Texas Instruments' ADC121C021 was used for the analog-to-digital conversion. The extra unused amplifier in the package was set as a voltage divided source follower to prevent errant behaviors or added noise.

Communication between the CCA's ADC and the motherboard occurred across an FFC using I^{2}C protocol. The FFC also provided the 3.3V, 5V, and ground supplies. Once the ADC values were read by the processor, the algorithm for value conversion could be performed.

5.2.3 CCA Results

The CCA was tested using the test airflow channel with a probe resistance of 3.46Ω. Using an airflow velocity range between 0 and 3.1 m/s, the reported ADC voltages varied between 2.87 and 3.16 V (Figure 20). Placing the probe in a sleeve lacking airflow revealed a noise floor of approximately 1 to 2 mV. This offered a great SNR for airflow velocities below 3 m/s. However, as the speed of the air increased beyond that point, the resulting voltage change diminished, causing the noise to become more dominant.
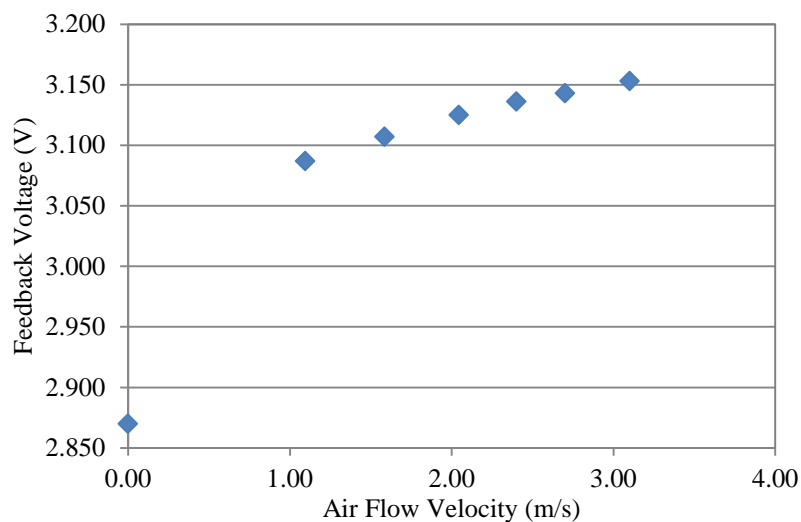
Figure 20:   CCA Output Voltage as a Function of Airflow Velocity

An additional problem also occurred during prolonged periods of time where the probe experienced no airflow. The steady-state temperature of the wire was often dependent on external factors, causing the behavior of the anemometer to lack consistency. While this issue is potentially solvable in firmware, the end result would be a reduction in accuracy. These problems, coupled with the power inefficiencies, encouraged the development of a CTA.

5.3 Constant Temperature Anemometer

A constant current caused overheating, which resulted in inaccuracies and wasted power. A CTA version of the device was developed to solve the accuracy and power problems of CCA.

5.3.1 CTA Simulation

The CTA circuit was first simulated in LTSpice to determine the range of stable behavior across multiple probe resistances and DAC voltage inputs (Figure 21). The reference leg of the bridge acted as a voltage divider on the output voltage of the DAC. Setting R_b and R_c equal to each other cut the DAC output voltage in half, allowing it slightly higher resolution control. Since the voltage generated at the reference leg was designed to be higher than the wire voltage, it was fed into the positive input of the amplifier. A gain of 10 is applied to the voltage difference. If the DAC voltage is held at a constant 1V and the probe resistance is stepped from 3Ω to 8Ω, the expected current through the wire is found to be approximately 69 mA to 36 mA, respectively.
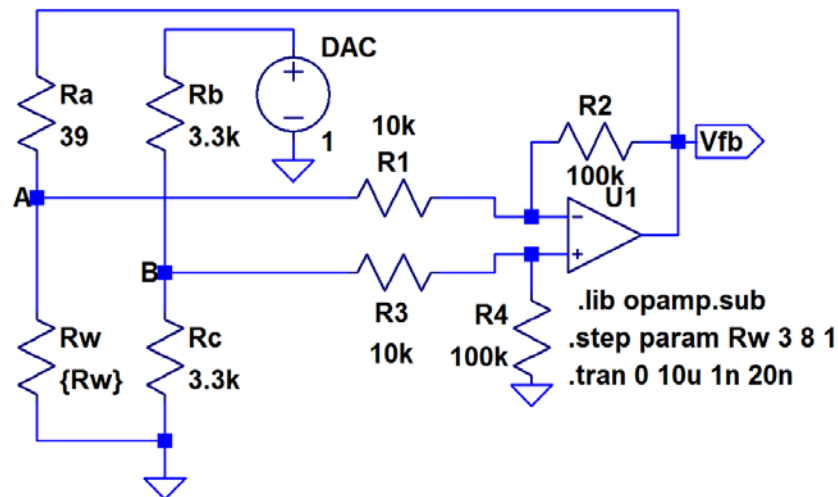
Figure 21:   LTSpice Simulation of the Basic CTA Circuit

The expected feedback voltages hit a maximum value of 2.87V when the

resistance is at its minimum. It is important to note that while the DAC voltage is held

constant in the simulation, it will vary based on the resistance of the wire to ensure proper

temperature compensation. Since the current through the wire decreases as its resistance

increases, the rate at which it overheats is diminished. This is necessary to ensure a

constant temperature is obtained during normal operation. However, if the starting

resistance of the wire is higher than its original calibration value, its overheat rate will not

match its previous levels, causing lower sensitivities and inaccuracies.

5.3.2 CTA Design

The circuit was designed using CadSoft's EAGLE PCB design software and

printed on a two-layer copper board. The board's dimensions were 30.55 mm by 13.3

mm and contained all components on a single side for ease of placement within the

PMON enclosure. A Flat Flex Cable (FFC) was used to extend power and protocol

signals from the motherboard to the CTA daughterboard. Due to the number of sensors

contained within a PMON unit, the I^2C protocol remained the viable option for adding

additional sensors. This same I^2C port was also used for two other daughterboards;

therefore, the anemometer daughterboard provided yet another FFC header to carry out

the supply and control signals. A right-angled 2-pin header acted as the probe's

connection point. The anemometer connected to the probe either via short wires or

directly, depending on the desired placement location of the board within the PMON

enclosure.

The CTA makes use of a digital-to-analog converter (DAC) for calibration

purposes. While the bridge still exists as per the original CTA design, the reference leg is

not connected to the feedback voltage. This moves more of the CTA operation into firmware, allowing for greater flexibility.

The components were selected based on simulated operating ranges, such as the wire current and feedback voltage. The MCP4728 from Microchip Technology was selected as the DAC for its 12-bit resolution and I^2C interface. Sourcing current to the wire required the use of a specialized amplifier. STMicroelectronics' TS9222 is a rail-to-rail high output operational amplifier capable of providing up to 80 mA to a load, which is more current than required according to the simulation. The ADC used in the design was Texas Instrument's ADC121C021. Similar to the DAC, this ADC was also 12 bits in resolution and was I^2C compatible.

The CTA EAGLE schematic, shown in Figure 22, implements the simulated circuit as shown in Figure 21. One minor difference between the simulation and the implementation is that the reference leg contains 10kΩ resistors instead of 3.3kΩ. This did not make any difference to the operation of the anemometer as the voltage division ratio remained the same.
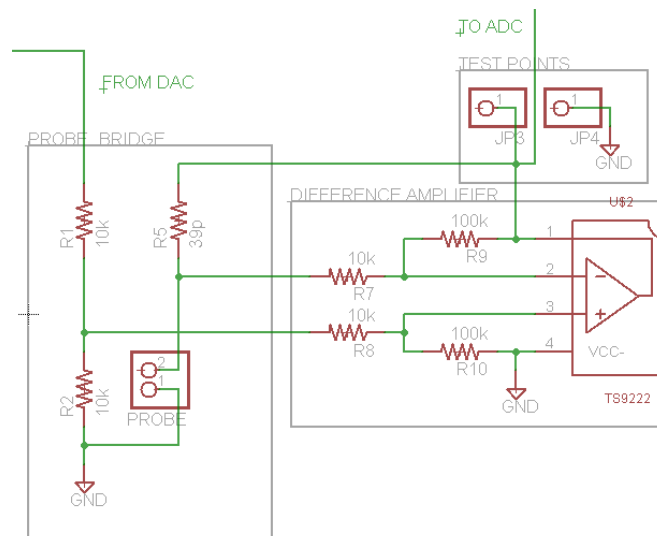
Figure 22:   CTA Eagle Schematic Excluding DAC, ADC, and FFC Headers

5.3.3 CTA Results

The CTA circuit was capable of obtaining the desired operating levels without saturating the ADC. However, stability of the circuit began to fade as the probe resistance was increased to levels beyond 5Ω. Increasing the DAC output may be required to assist in stability for highly resistive probes. Probes with resistances exceeding DAC compensation will need to be replaced.
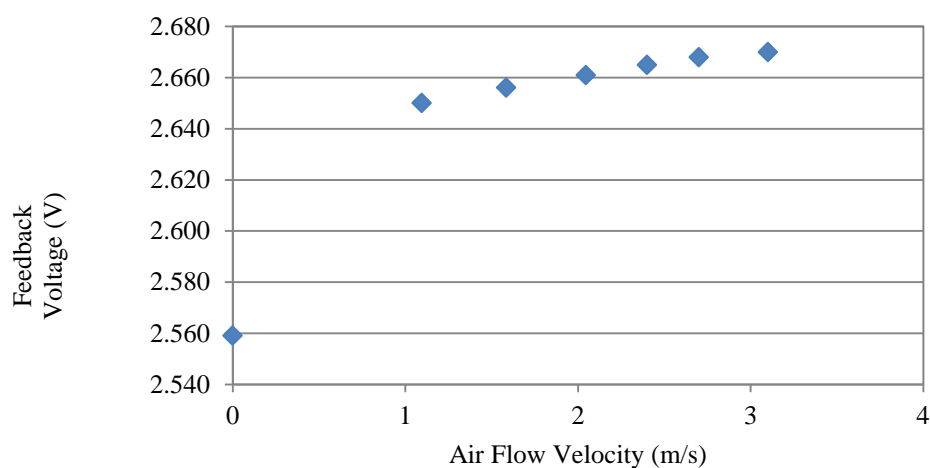
Figure 23:   CTA Feedback Voltage as a Function of Airflow Velocity

The feedback voltage for a given probe varied across a range suitable for obtaining accurate airflow measurements. Using a 2.67Ω probe 3 mm in length, feedback voltage was plotted as a function of airflow velocity (Figure 23). A paper sleeve was placed over the probe to test no flow conditions. This showed that equilibrium between overheating and alternative heat transfers was accomplished at around 2.67V. When placed in the test channel, airflow velocity was varied by changing voltage to the fan. The results showed a non-linear relationship between the voltage and flow velocity, as expected. The voltage appeared to asymptotically approach 2.74V as the speed was increased above 6 meters per second.

Expectedly, the voltage feedback was not consistent for all starting resistance values for the different probes. A decline in the operating point appeared to drop logarithmically as the value of the resistance increased.
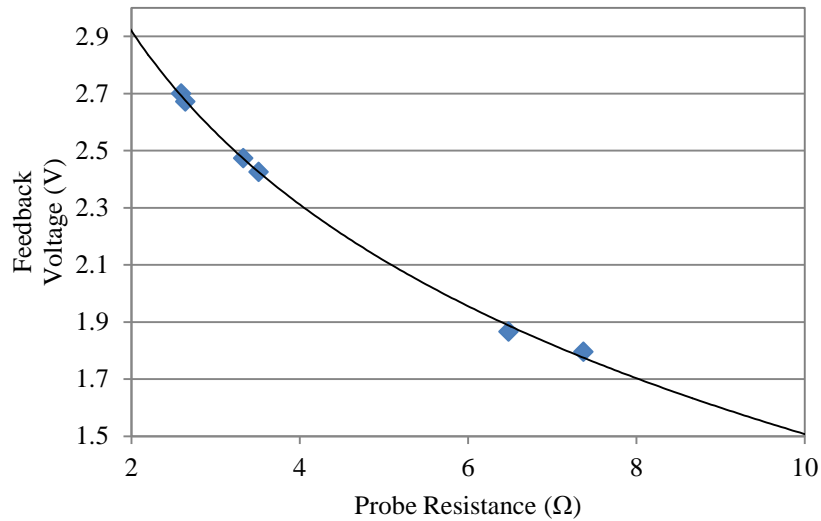
Figure 24: **Operating Feedback Voltage at No Flow Conditions as a Function of Probe Starting Resistance**

A lower operating point also indicates a lower operating temperature. Consequently, a higher probe resistance negatively impacts the airflow velocity resolution of measurement. A higher DAC output can be applied to assist in off-setting the loss of sensitivity.

CHAPTER 6: FIRMWARE DESIGN

This chapter covers the implementation of the OPC and anemometer firmware. The effects of airflow velocity on particulate data characteristics are shown. Methods of measurement compensation and fan control are then discussed.

6.1 Optical Particle Counter Firmware

The OPC firmware was designed as part of previous research and the majority of the code remained unmodified during development of the CTA compensation method. The unchanged portions of the code are not thoroughly discussed in this research and can be found in [6]. The modified areas, including the original particle counting method and the proposed anemometer enhanced method, are discussed.

6.1.1 Original Counting Method

The original OPC is designed with a single photodiode sensor for the capture of scattered light. Two amplifiers are set on the output of the photodiode. The first amplifier is labeled "small particle amplifier" and has a larger gain than the second amplifier, which is labeled "large particle amplifier." The scaled output from the small particle amplifier is used to trigger the measurement algorithms and to determine the validity of a pulse as a particle count. The large particle amplifier's gain is set relatively low in order to prevent ADC saturation. Particulate triggering and identification required the use of several variables generated in calibration.
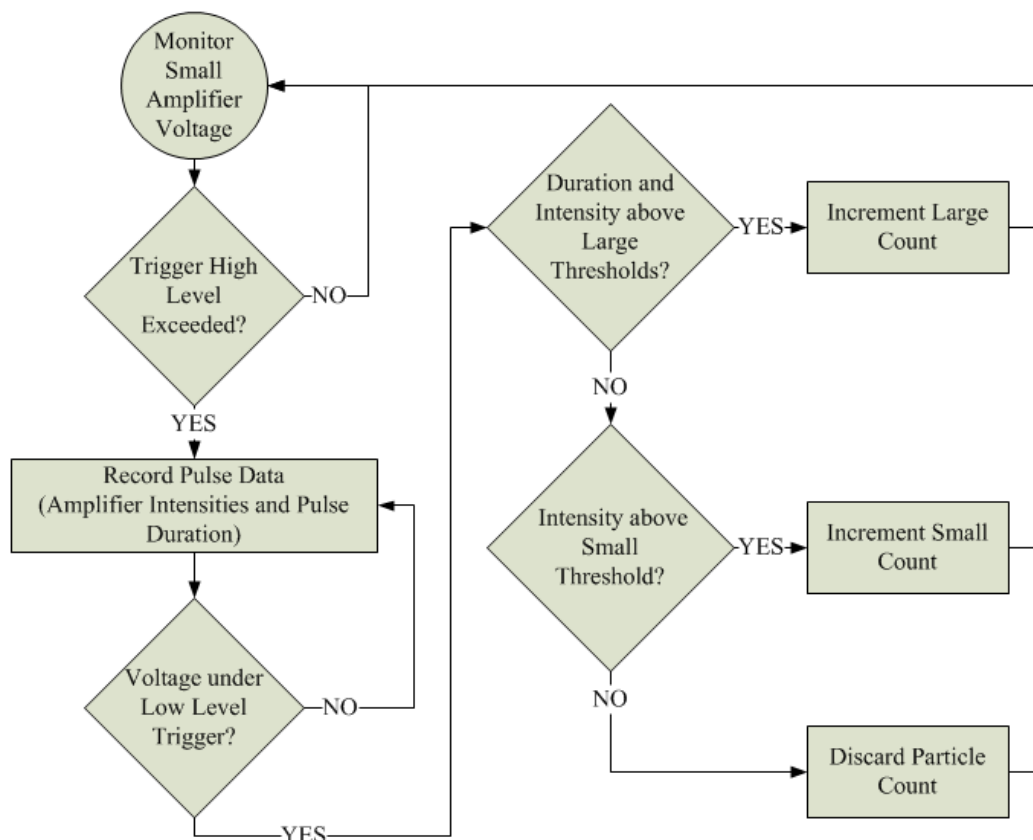
Figure 25:   Simplified Particle Processing Algorithm Flowchart

Similar to the CTA, the OPC requires experimental data and a gold standard for proper calibration. Comparisons between the gold unit's count numbers and the non-calibrated unit's count numbers are performed using MATLAB scripts. The output of these scripts is a table of several values that can be set in the system configuration as calibration factors. Following Figure 25, a trigger value dictates when a pulse signifying a particle is large enough to begin the measurement process. Once the measurement process is complete, threshold values are then compared to the pulse intensity and duration in order to assign the count a bucket: small or large. Based on the counting interval, the buckets are periodically scaled by values to determine the ambient particulate concentration. After scaling, the results are reported and then the buckets are emptied.

Part of the calibration process for a PMON includes the addition of a sample

scalar applied to a bucket prior to reporting the concentration results (Figure 26). This

sample scalar primarily represents a means of scaling the volume of air sampled to

another volume of the desired metric (e.g., liters). However, this sample scalar can also

account for the difference of several possible variables between the gold standard and a

unit undergoing calibration. For example, one PMON may contain a laser with a lower

than normal output power. Consequently, really fine particles may produce pulse

amplitudes smaller than what is determined to be noise. On the other hand, a unit could

have a more powerful laser and produce higher pulse amplitudes. The calibration method

would ensure that all units could agree on an ambient concentration level by adjusting the

sample scalars and threshold values for each.
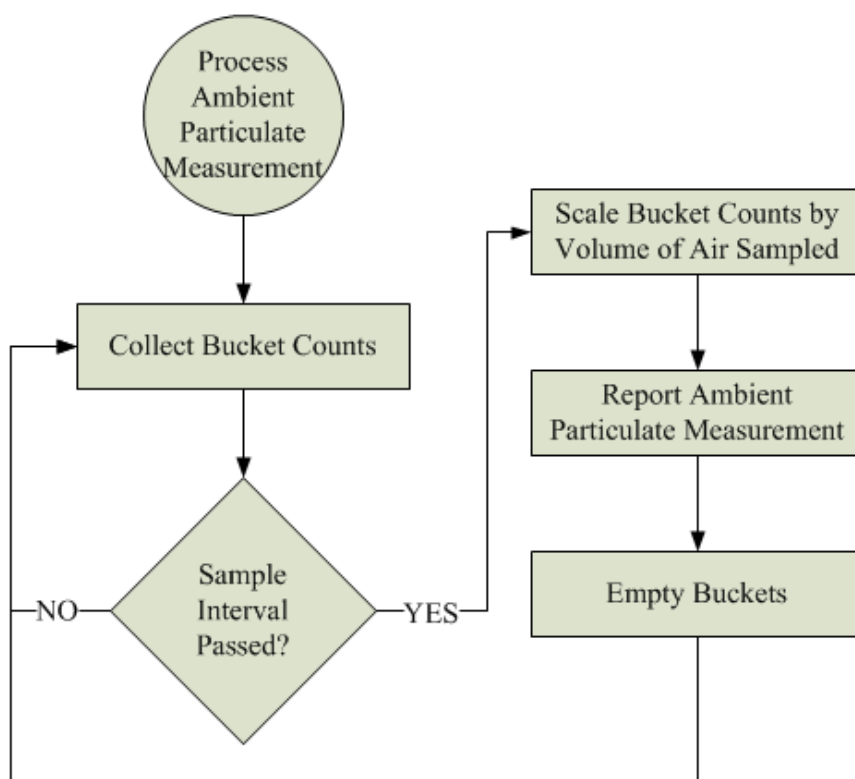
Figure 26:   Particle Count Sample Scaling Flowchart

6.1.2 Effects of Varying Airflow on Particle Counts

Another physical variance that is compensated through the sample scalar is the airflow velocity. When the units were previously designed, they were assumed to operate with constant laminar flow through the channel. However, the volume of air being sampled, loosely expressed in cubic feet per minute (CFM), varies alongside the airflow velocity. In this instance, using a static sample scalar no longer provides accurate data.

If the particulate is assumed to be evenly distributed and the air that carries it incompressible, then a change in the airflow velocity should result in a proportional change of the numbers of particles traveling through the beam. This is reflected in the identity of volumetric flow rate where

$$Q = V_f A. \tag{12}$$

In Equation (12), Q represents the volumetric flow rate (e.g., CFM), V_f is the velocity of the fluid, and A is the cross-sectional area through which the air passes. Therefore, any deviation of the airflow velocity from what was used during OPC calibration should be reflected in the particle count linearly.

In order to verify the validity of this assumption, two units were placed in the particle chamber in a way similar to Figure 10, Section 3.1.2. Unit A was used as the control and Unit B was enhanced with a calibrated hot-wire anemometer. The chamber was initially evacuated of all particulate and 0.6 μm PSL was added to the collision nebulizer. An oscilloscope probe was placed across the output of the small particulate amplifier and the ground plane of Unit B's motherboard so that the pulse characteristics could be monitored. Using both the internal and external fan, airspeed velocity through Unit B's OPC channel was brought to approximately 5 m/s. Particulate measurements

were then captured wirelessly as the power to the fans was lowered every several minutes.

Figure 27 shows the particulate concentration measurements of Unit A and Unit B during the experiment. The airflow velocity through Unit B was also plotted on the secondary axis for ease of comparison. At a glance, the relationship between airflow velocity and PM measurements does appear to be fairly linear for velocities under 5 m/s. The error between the units regarding PM concentration measurements is considerably large for airflow values much greater or less than 3 m/s. In one of the worst cases, when the airflow velocity was nearly 5 m/s, the difference was about 10,000 PPL. At that airflow velocity, for any given particle concentration inside the chamber, Unit B should produce approximately 140% the value that of Unit A. At the opposite end, where the airflow velocity drops below 1 m/s, the difference was also about 10,000 PPL, or 60% that of Unit A's measurement.
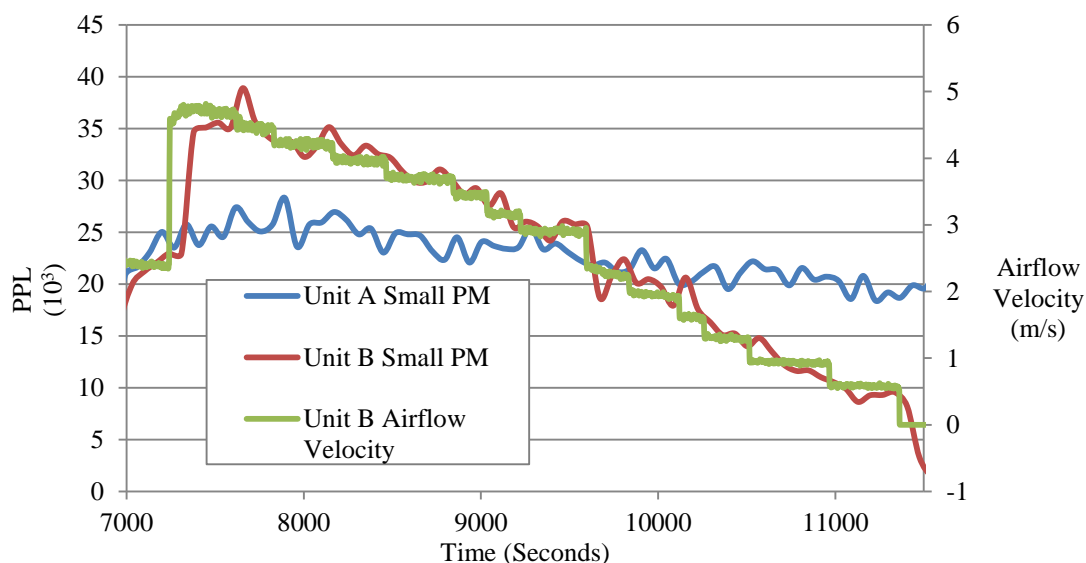
Figure 27:   Effects of Varying Airflow on Particulate Measurements

The change of airflow velocity also affected the pulse characteristics generated by each particle. Figure 28 reveals that a higher airflow velocity also results in shorter pulse amplitudes. As the velocity approaches 5 m/s, the average pulse height was only approximately 1.2V. This can have dire effects on the triggering and verification portions of the original particle counting method. Once the average pulse height falls below the OPC calibration threshold, most of the particles will be ignored. This is most likely the explanation to the lowered particle count seen on Unit B in Figure 11 of Section 3.1.2.
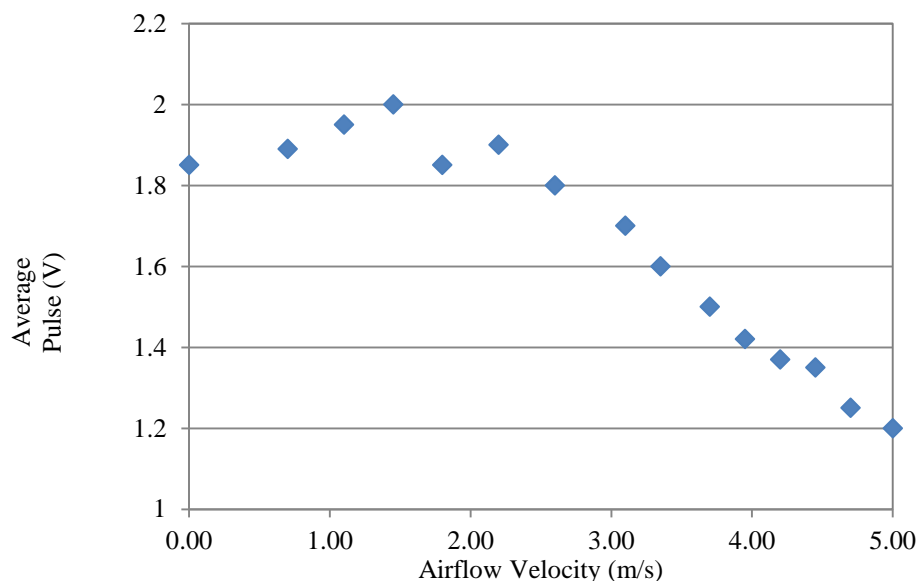
Figure 28: **Effects of Varied Airflow Velocities on Average Particle Pulse Amplitude**

Another characteristic affected by the airflow velocity is the pulse duration. In [6], the pulse duration was used as a feature to assist in differentiating between particle sizes. As the velocity of the particle traversing the beam increases, the duration of the pulse decreases. This trend can be noted intuitively and is confirmed in Figure 29. In addition to misclassification, shorter pulse durations may also lead to an increased volume of the beam used to accept particles. For example, if a large particle with a normal velocity

passes through a portion of the beam that is far from the focal point, the result will be a short to medium pulse height with a long duration. However, if the particle is moving with a higher velocity, the generated pulse may still be a small to medium pulse height but with a shorter duration. Consequently, it will be classified as a small particle and not discounted as being outside the valid portion of the laser beam.
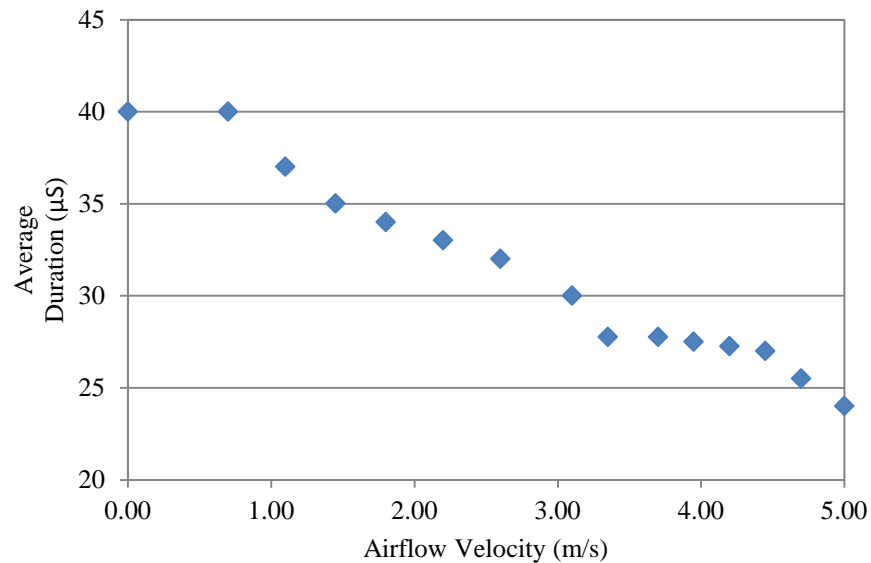
Figure 29: **Effects of Varied Airflow Velocities on Average Particle Pulse Duration**

The Reynolds number is also affected by the airflow velocity. The hydraulic diameter of the airflow channel is denoted

$$D_H = \frac{4A_c}{P_c} \tag{13}$$

where A_c is the cross-sectional area of the channel and P_c is the wetted perimeter of the channel. Given that the channel dimensions are 6 mm by 10 mm, d_h is calculated as 7.5 mm. The hydraulic diameter can then be substituted into the Reynolds equation along with the airflow velocity. If the ambient air is assumed to be of static temperature, then its kinematic viscosity, ν, should also remain static. Using Equation (5) in Chapter 4 with a

varied airflow velocity, the Reynolds number can be plotted for different temperatures (Figure 30).
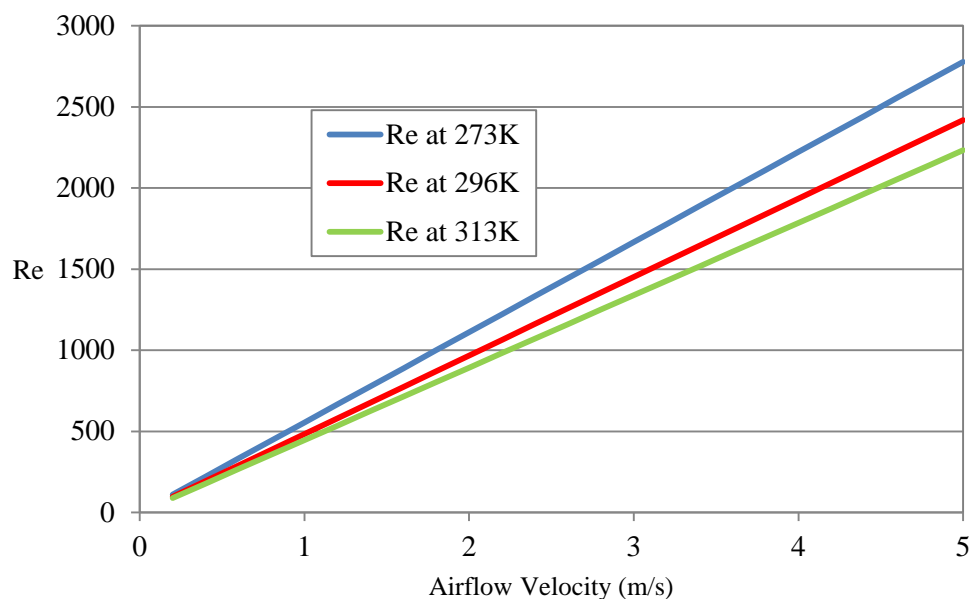
Figure 30:   Reynolds Number for Varied Airflow Velocities at 3 Operating Temperatures

Assuming laminar airflow for $Re < 2300$, an airflow velocity 3 m/s or less will result in laminar flow through the channel. As the airflow velocity approaches 4-5 m/s (temperature dependent), the airflow enters the transient region. This transition may be characterized as a combination of turbulent and laminar flows. Since the airflow velocity is greatest in the center of the channel, turbulent conditions may be occurring near the laser focal point at the higher airflow velocities.

6.1.3 Particle Count Compensation

To account for airflow changes, the calibration and measurement values require real-time updating. The sample scalar can be used to compensate for sample size changes while the intensity and duration measurements (Figure 31) can be used to compensate for pulse voltage levels.
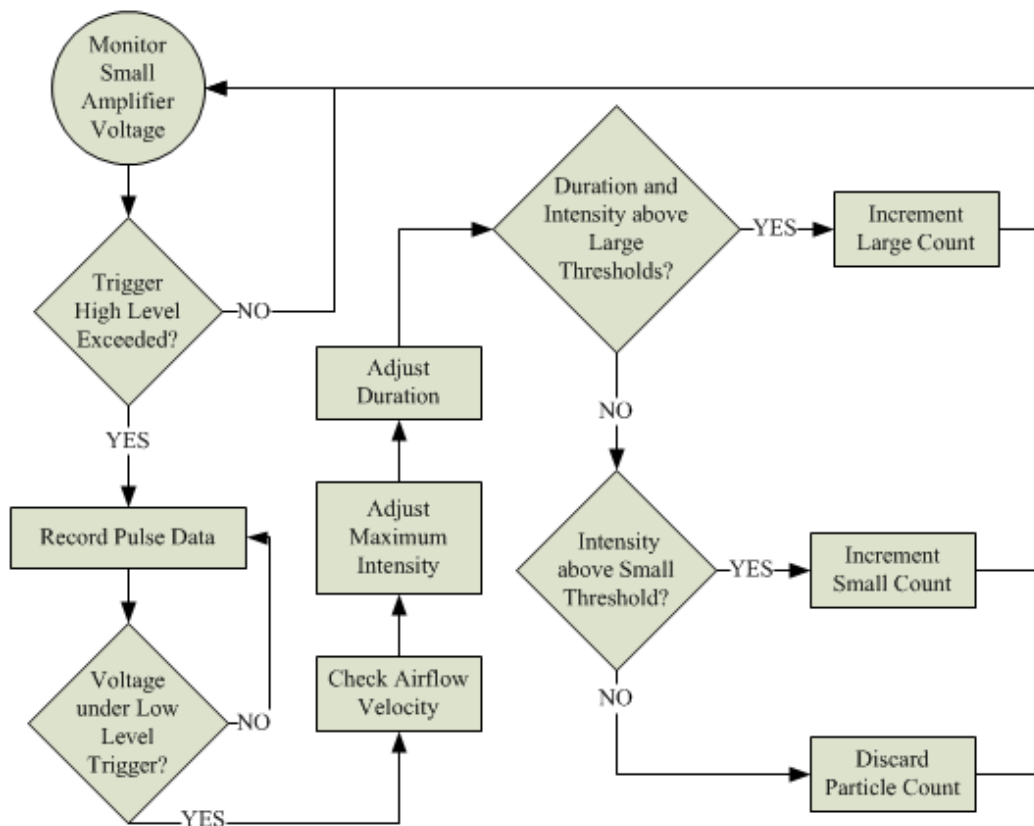
Figure 31:   Particle Processing Compensation Flowchart

Since the relationship between the amount of air being sampled and the airflow velocity is approximately linear, the sample scalar is simply multiplied by the ratio between the desired airflow velocity and the current airflow velocity. The desired airflow velocity is obtained during the OPC calibration process. During the OPC calibration, the airflow velocity should be as static as possible. Upon successful calibration, the average airflow velocity should be recorded with other calibration values so that it can be used for comparison with the current airflow velocity at a later time.

As shown in Figure 32, the amount of time between bucket reports needs also to be considered when applying the ratio to the sample scalar. If only the immediate airflow velocity is considered, then a bucket may be scaled inappropriately. For instance, the period of a bucket's particle count accumulation may be spent while the airflow velocity

is at a static value. If the airflow velocity experiences a sudden change immediately prior to bucket reporting, the bucket's total count will be scaled by that new airflow velocity. Therefore, the airflow velocity should be integrated for the duration of the bucket's accumulation period. This is easily accomplished by maintaining a local value in the anemometer code. Each airflow velocity sample should be added to a pool while a counter is incremented. Then, when the bucket is preparing to report the PM concentration, the total volumetric airflow can be determined for the sample. The airflow velocity integrated value is then reset in preparation for the next bucket.
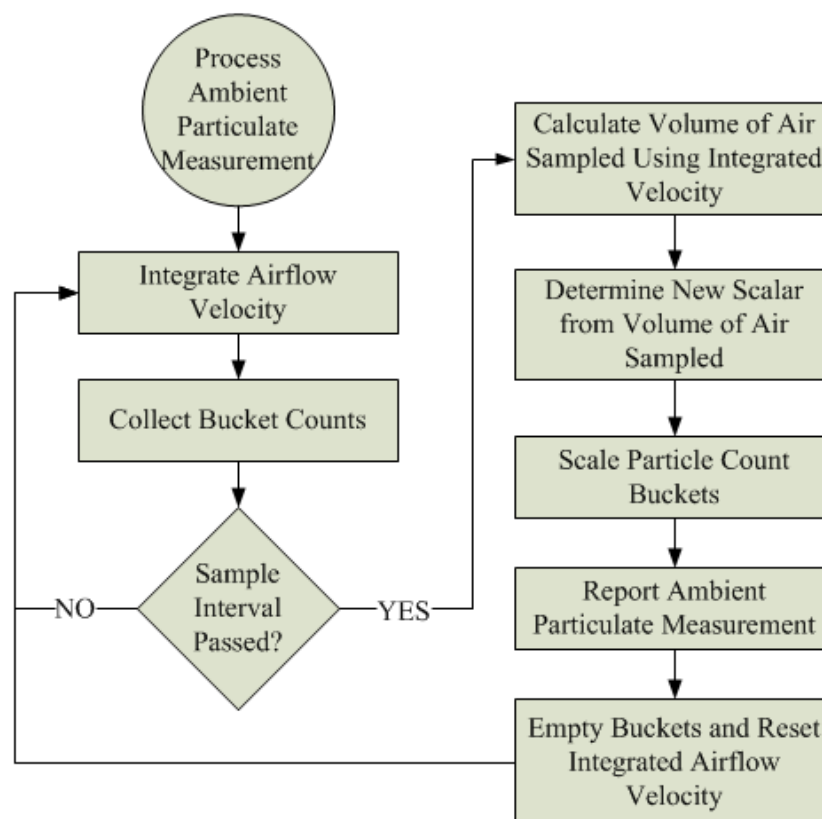
Figure 32:   Sample Scaling Compensation Flowchart

To correct for the discrepancy involving the pulse amplitudes, the airflow velocity needs to be constantly monitored. In the event the velocity exceeds a value capable of driving the majority of pulse heights below the triggering threshold, the system will need

to adjust accordingly. Based on Figure 28, this velocity appears to be above 3 m/s. The lost pulse amplitude can be plotted as a percentage of the expected average pulse amplitude for airflow velocities between 3 and 5 m/s. Using the equation shown in Figure 33, the estimated error can be found for y if the airflow velocity is substituted for x. A corrective multiplier can then be easily found by adding the estimated error to one. As the airflow velocity exceeds the 3 m/s threshold, this simple multiplier should be applied to the peak value obtained for a pulse sample.

$$y = 0.1346x - 0.2951$$
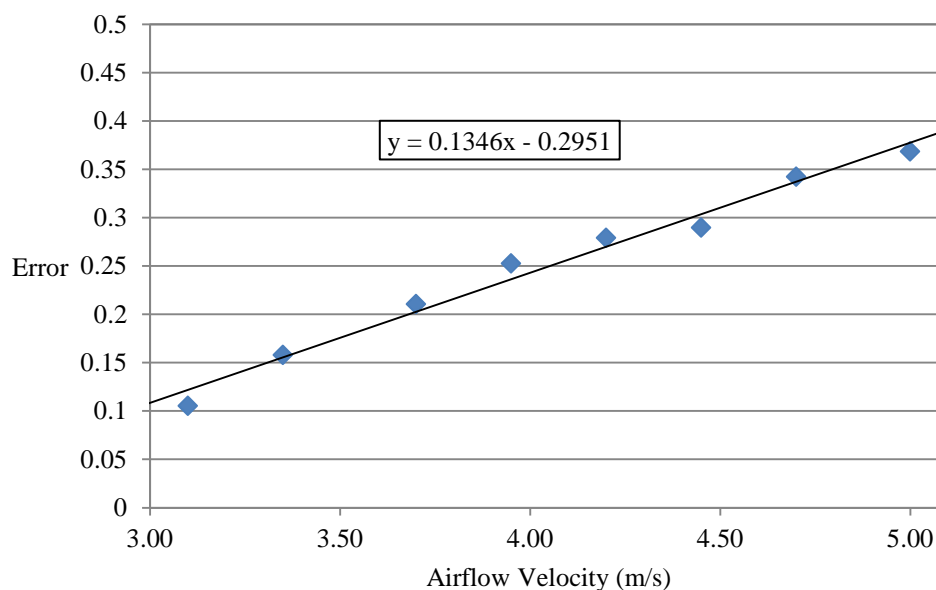
Figure 33:   Pulse Height Error due to Increased Airflow Velocities

6.2 Hot-Wire Anemometer Firmware

The hardware for the anemometer is simple in its functionality: maintain proper wire temperatures and report the feedback voltage to the processor. Consequently, the software of the anemometer is where the bulk of the measurement work is done. First, the processor must determine the probe resistance without overheating the wire. Next, a reference voltage based on probe resistances discrepancies must be calculated and applied to the circuit for wire overheating. Lastly, ADC readings must be properly

converted to airflow velocity values in order to update the fan's feedback control and to compensate particle counter readings.

6.2.1 Sensor Framework

Adding a sensor to the PMON's framework has been made relatively easy due to the existing modular implementation. Basic data structures require the addition of function pointers to the sensor's initialization and task functions. Sensor type, data type, and sensor model need to be defined in all appropriate areas. Adding the sensor to the PMON platform and enabling it is the last step before the initialization and task functions are called during normal operation.

All registered and enabled sensors are initialized whenever the system is turned on. The initialization process for each sensor is based on that sensor's initialization function. For the anemometer (Figure 34), the DAC and ADC each need to be initialized by setting all structure values and pointers. The calibration data is then retrieved and applied to the appropriate variables. Detecting the wire's starting resistance is also handled during initialization since the wire has yet to be heated. The initial resistance of the wire is then used to calculate the reference voltage generated by the DAC. Once the anemometer and all other sensors have completed their initialization processes, the sensor task function can be called.
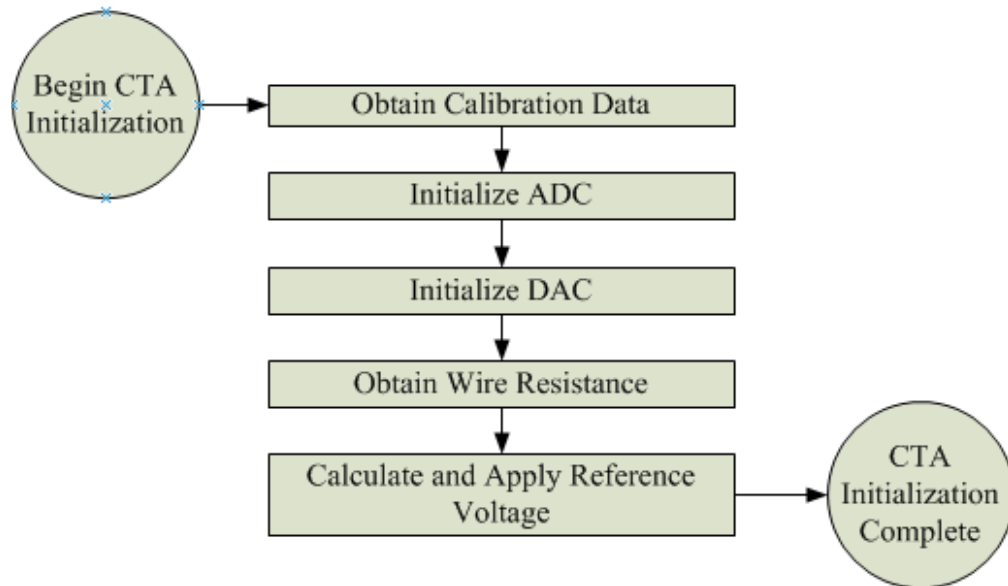
Figure 34: **CTA Initialization Flowchart**

   The anemometer's task function is called in the PMON sensor task loop. As

shown in Figure 35, the function starts an ADC read if the task flag is set. If the task flag

is not set, then the function checks the ADC for a completed measurement. If new data

has arrived, the function reconstructs the voltage read from the 12-bit ADC value. Using

calibration data, the voltage is then converted to airflow velocity. A flag is then set to

alert the data manager of the presence of new data so that it can be routed to all

appropriate destinations.
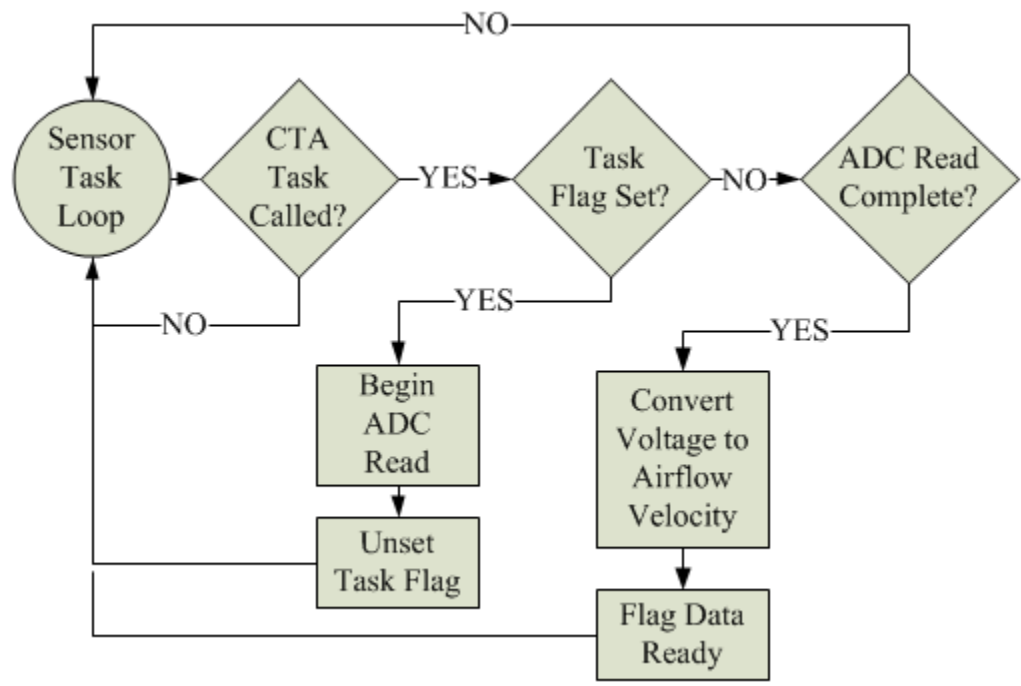
Figure 35:   Anemometer Sensor Task Flowchart

The interval at which the sensor's task function is run is defined as a parameter that can be changed in the SD card. As shown in Figure 36, a scheduler runs based on a hardware timer and determines when sufficient time has passed before activating a flag for a given sensor. Each run through the PMON's main task loop checks for flagged sensors and then activates their task function.
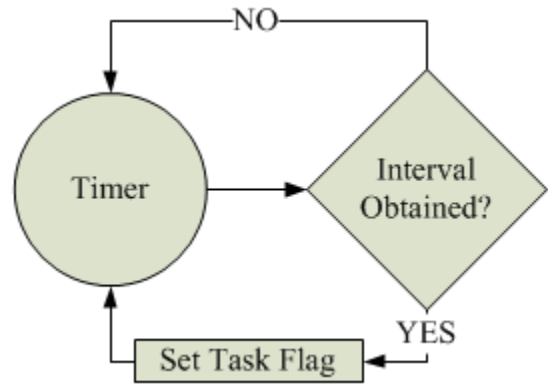
Figure 36:   Sensor Interval Flowchart

Running a lower interval for a sensor produces data more quickly. Faster data collection is capable of capturing higher frequency variances in the sensor measurements. As a tradeoff, faster data collection requires more data storage and also consumes more processor time.

6.2.2 Probe Resistance

Each probe has shown differing resistances based on the actual length of the wire. Additionally, the hand-soldering method employed in probe construction can lead to wire damage. Variation in probe resistances causes difficulties in determining the wire temperature at any given time since Equation (1) requires R_0 and T_0 to be known a priori. This problem can be solved by simply working backwards from the ADC output to all known circuit factors.

The temperature of the wire, before the CTA is run, should be about the same as that of the ambient temperature. Thus, a few thermistor samples can be averaged to find T_0. Finding R_0 is a more complicated process since it requires reading the ADC prior to running any large amounts of current through the wire. Using a low reference voltage with the DAC prevents the wire from overheating, but a reference voltage too low results in lower resistance measurement accuracy.
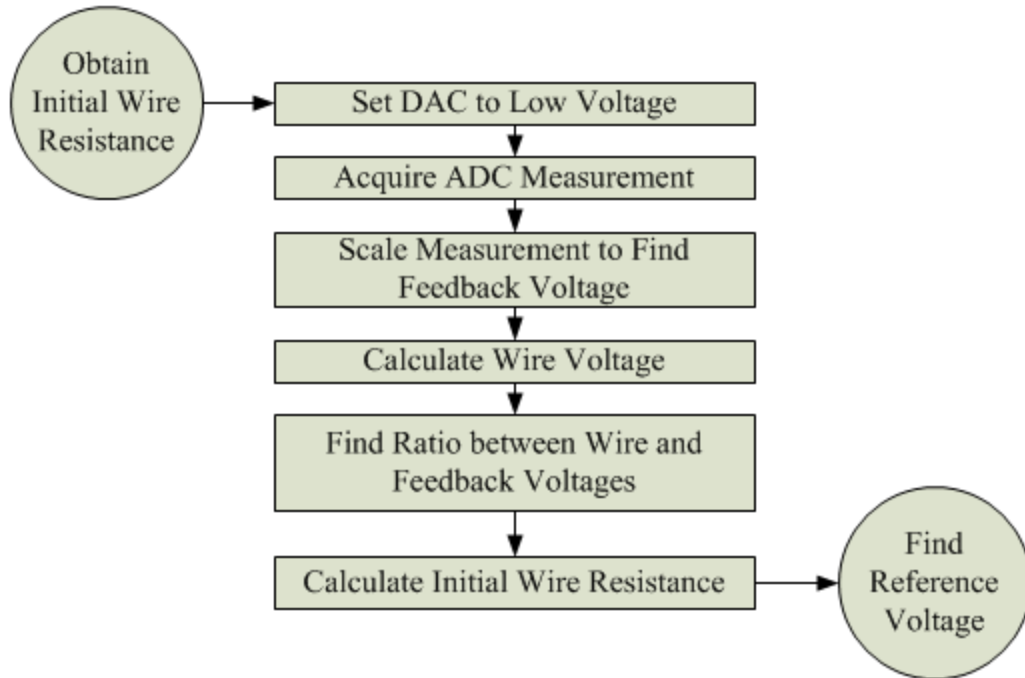
Figure 37: **Initial Wire Resistance Measurement Flowchart**

To find the starting wire resistance R_0, the ADC voltage measurement must first be divided by the gain applied at the differential amplifier. The result is the difference between the reference voltage V_{ref} and the voltage across the wire V_w. Subtracting this voltage difference from V_{ref} yields V_w. Since the value of the resistor (R_a, see Figure 21, Section 5.3.1, CTA Simulation) set in series with the wire is already known,

$$R_0 = \frac{\frac{V_w}{V_{fb}} R_a}{1 - \frac{V_w}{V_{fb}}},$$

(14)

where V_{fb} is the feedback voltage that is found by reading the ADC. Having R_0 now provides a means of determining the operating region and maintaining calibration data for longer periods of time.

Using a reference voltage of 30 mV, the anemometer is shown to be successful in estimating the probe resistances (Table 1). One should note that as the resistance of the

probe increases beyond 4Ω, the algorithm begins to slightly overestimate. This becomes

much more of a problem when the resistance reaches even higher values. However, a

probe should be replaced when above a certain threshold. Once the resistance is

determined, it is inserted into the sensor firmware. The reported value should be checked

periodically to determine if a probe is due for a replacement.

Table 1: **Resistance Estimation Results during Anemometer Initialization**

Probe #:	1	2	3	4
Actual Resistance (Ω):	3.57	8.26	3.33	4.82
Estimated Resistance (Ω):	3.55	8.63	3.32	4.89
Error (Ω):	-0.02	0.37	-0.01	0.07
Error (%):	-0.56	4.48	-0.42	1.45

6.2.3 Reference Voltage

The reference voltage V_{ref} directly affects the temperature setting of the wire and

is used to compensate for wire resistance discrepancies. In the event that the starting wire

resistance R_0 is lower than the ideal resistance, V_{ref} needs to also be lower to ensure a

consistent operating temperature. The same holds true for the inverse: a resistance greater

than ideal requires a higher voltage. A baseline voltage needs to be determined

immediately after obtaining R_0. The starting resistance is necessary to calculate the

voltage required for the operating temperature.

The operating temperature of the wire is controlled by the DAC output voltage. A

higher DAC output results in a higher V_{ref}, which then increases the voltage difference.

Consequently, V_{fb} is also increased, raising the power delivered to the wire. The

temperature of the wire rises to compensate, increasing its resistance as demonstrated in

Equation (1). Based on these physical parameters, an equilibrium is found once the resistance of the wire produces a voltage that nearly reaches V_{ref}.

A higher overheating of the wire results in a more sensitive anemometer but also requires more power. Wire heating too much is also affected more by conductive and radiation heat transfers. Therefore, the probe's sensitivity must be balanced with its power consumption. Ideally, the wire would obtain overheat temperatures just barely sensitive enough to capture potential variances at a resolution allowing for accurate PM measurement compensation.

As the wire's base resistance increases, its sensitivity drops despite an approximately static power of 11 mW to 12 mW. Figure 38 is the voltage versus airflow response from a probe with a resistance of 6.5Ω. As can be seen, the resolution of the ADC begins to falter as the airflow peaks around 5 to 6 meters per second. Additionally, the total voltage swing from maximum fan speed to no air movement is a mere 11 mV. This is a significant loss of data from what was seen in Figure 23 in Section 5.3.2.
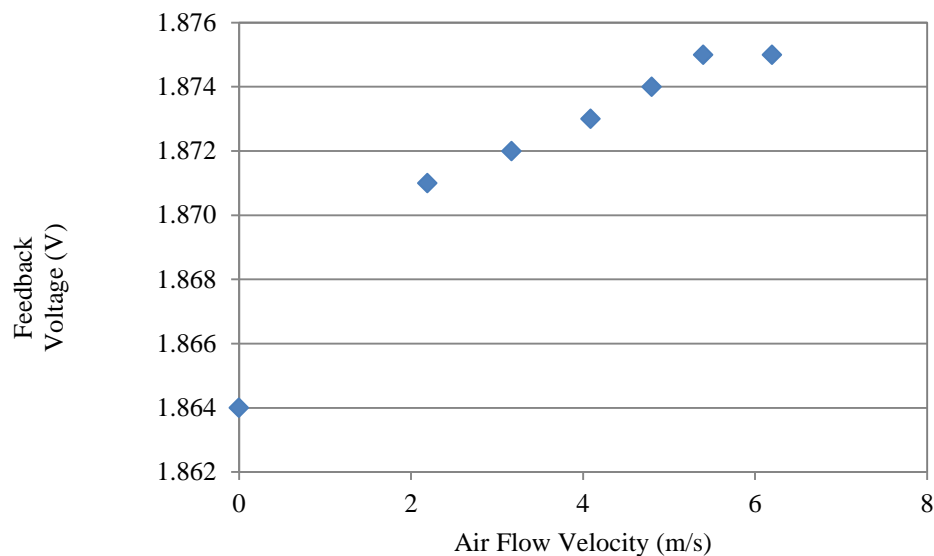
Figure 38:   Feedback Voltage of Airflow for Highly Resistive Probe (6.5 Ω) with DAC Output of 1 V

Increasing the DAC output from 1 to 1.4 V improves the sensitivity. Figure 39 shows that the voltage swing ranges over approximately 50 mV, thus providing 5 times the amount of sensitivity. Additionally, the probe can now differentiate between the higher airflow velocities. As a tradeoff, the power consumption more than doubles, ranging around 23 mW at the maximum fan speed. While this sensitivity level provides sufficient resolution, the power consumption is barely tolerable for this platform. A probe with much lower resistance of around 2 to 3Ω should be used for optimal performance.
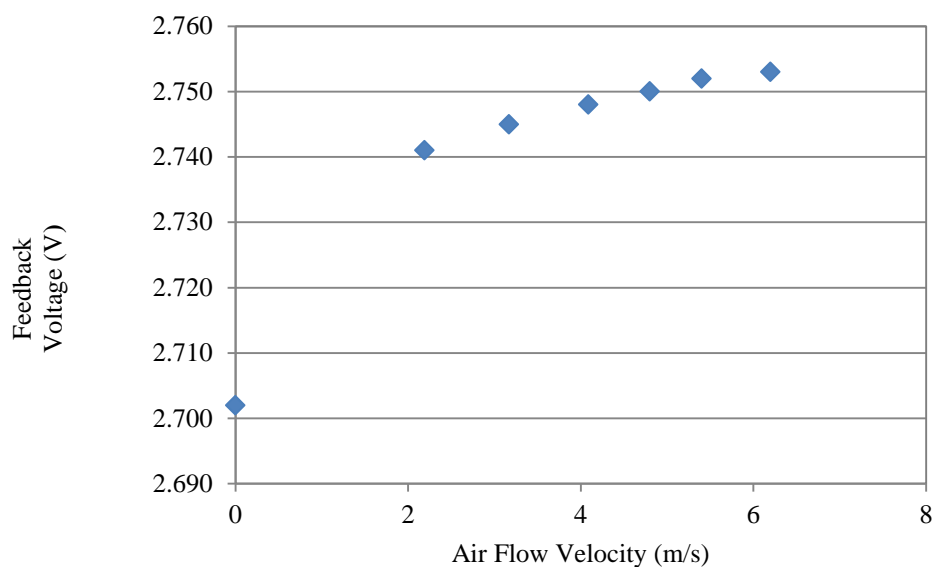
Figure 39: **Feedback Voltage of Airflow for Highly Resistive Probe (6.5 Ω) with DAC Output of 1.4 V**

For probes operating in the low resistances, small adjustments to the DAC voltage are required to prevent the need for recalibrations. These adjustments should be found using the difference between the resistance at time of calibration and the resistance found during initialization. Any alteration to the anemometer caused by a change in the resistance should be remedied by the amount added to the DAC.

6.2.4 Anemometer Calibration

The calibration process for the hot-wire anemometer is significant to the operation of the anemometer. Unfortunately, due to the indirect relationship between convective heat transfer and the voltage feedback in the CTA circuit, the calibration must be done against reference airflow velocities [33]. The complexity of this relationship is apparent when referencing Equation (10) in Section 4.1. Several of the variables are temperature dependent, and the accumulated error in any of the design measurements can become problematic. However, it can be seen that many of the constants can be collapsed into the A and B coefficients, which can then be found experimentally. This is demonstrated in the simplest form of King's Law [34]:

$$E^2 = A_1 + B_1 U^n. \tag{15}$$

In Equation (15), E is the feedback voltage and U is the airflow velocity. The coefficients A_1 and B_1 must be obtained experimentally through calibration. The exponent n is generally varied from 0.1 to 0.5 during experimentation in order to find the best value for linearization. However, this form of King's Law does not take the ambient temperature into consideration. Temperature compensation can be accomplished by multiplying the right side of the equation with the difference between the wire temperature T_w and the ambient temperature T_f:

$$E^2 = (A_2 + B_2 U^n)(T_w - T_f) \tag{16}$$

Given the linear relationship between the wire's resistance and its temperature, the difference between T_w and T_f can be replaced with the difference between the wire's current resistance R_w and its resistance at the temperature of the fluid R_f [34]:

$$E^2 = (A_3 + B_3 U^n)(R_w - R_f) \tag{17}$$

Using a DC power supply, voltage to the fan was dropped from 5 to 2 V in 0.5 V increments. Placing the Extech SDL350 [8] into the test channel, airflow velocities were found for each voltage level of the fan. Immediately following, the Extech probe was replaced with the custom hot-wire anemometer probe being calibrated. The process was repeated while the feedback voltage for each fan speed was recorded. Using Excel, it was found that a linear fit was achieved for A_3 equal to 6.5484 and B_3 equal to 0.464. This was accomplished using an n equal to 0.2 and can be seen in Figure 40. The linear fit appears to work fairly well, although it begins to underestimate the airflow at the highest voltages. The probe resistance was 4.61Ω.
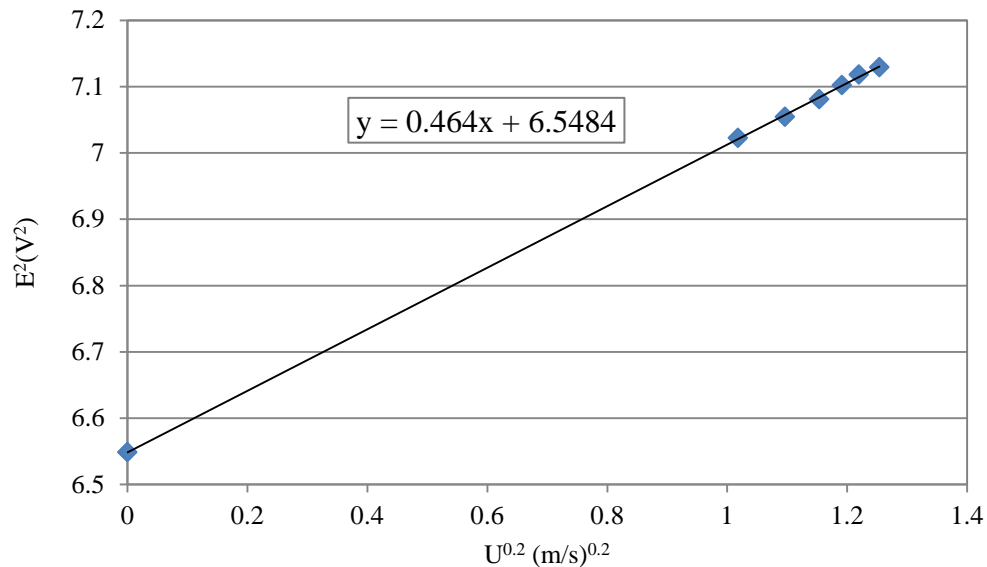
Figure 40: **CTA Calibration Using *n* = 0.2**

6.2.5 Airflow Conversion

Equation (17) is far simpler than Equation (10). Since the airflow velocity U is required, the equation needs to be rearranged:

$$U = \left(\frac{E^2}{B_3(R_w - R_f)} - \frac{A_3}{B_3} \right)^{\frac{1}{n}} \qquad (18)$$

Using Equation (18), the airflow conversion process can be completed (Figure 41). This process begins by reading the anemometer ADC. The value is then converted to the actual voltage by multiplying by the reference voltage (3.3 V) and dividing by 2^{12}. The result is then squared and scaled slightly by the deviation in temperature. The deviation in temperature is found by subtracting the current ambient temperature from the temperature of the wire at the time of calibration. The calibration scale and offset is then applied to the updated voltage. The exponent is then applied.

Floating point calculation using an embedded platform lacking floating point hardware is fairly slow. This can be circumnavigated by leaving it out of Equation (18) and then multiplying U with itself a particular number of times. Note that this method only works if the inverse of n is an integer. For example, if n is equal to 0.2 then U will need to be exponentiated by 5. On the other hand, if n is equal to 0.3 then U will need to be exponentiated by 3.333. In the course of this research, it was found that n was generally equal to 0.5 for the test channel probes and 0.2 for the OPC flow channel probes, both of which permitted the use of this technique.

The variable R_f is found using the method described in Section 6.2.2, Probe Resistance, during anemometer initialization. The resistance of the wire R_w is found during normal run-time operation at each anemometer sensor poll. The difference between the two acts as a scalar that assists in accounting for variances in starting wire resistances and air temperatures. Either the difference in temperature or the difference in resistance can be used to compensate.
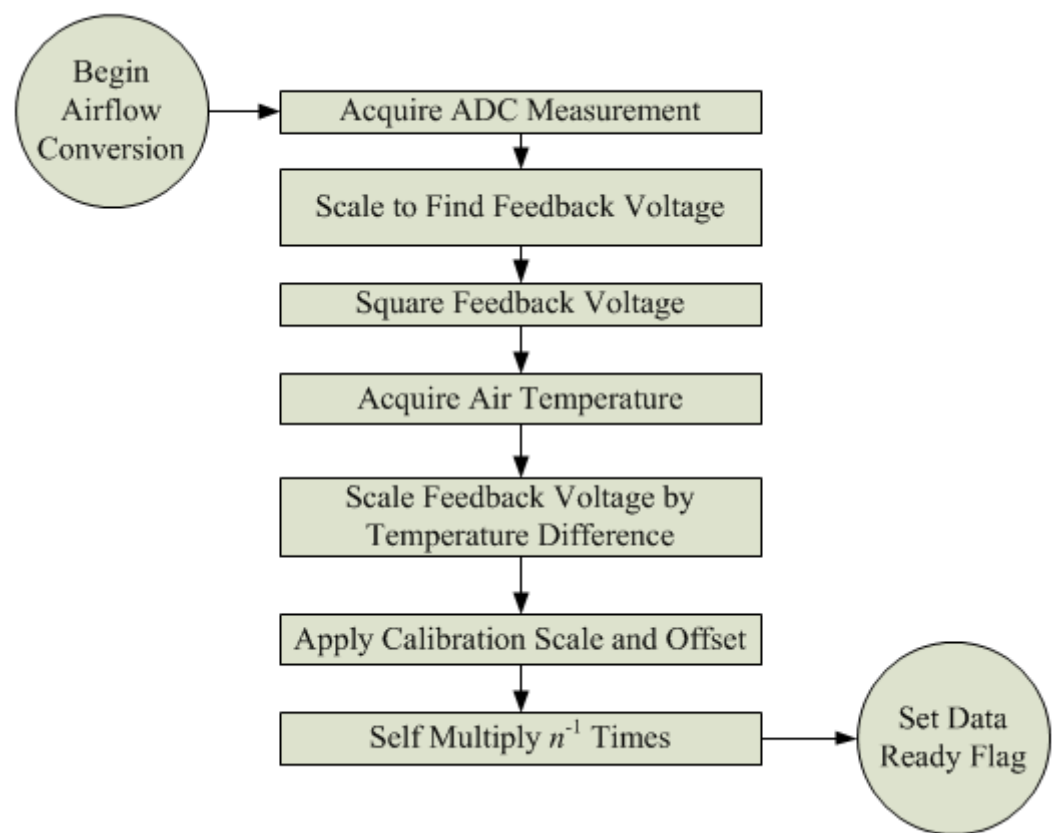
Figure 41:   **Airflow Conversion Flowchart**

Prior to temperature compensation, the CTA was left running overnight as the ambient temperature was slightly varied. Both the feedback voltage and temperature were recorded. Figure 42 reveals the inverse correlation between the voltage and the temperature. For every degree Celsius (or Kelvin) that changed in the ambient temperature, the feedback voltage demonstrated an approximately 2 mV change in the other direction. The difference between R_w and R_f will have to be scaled accordingly.
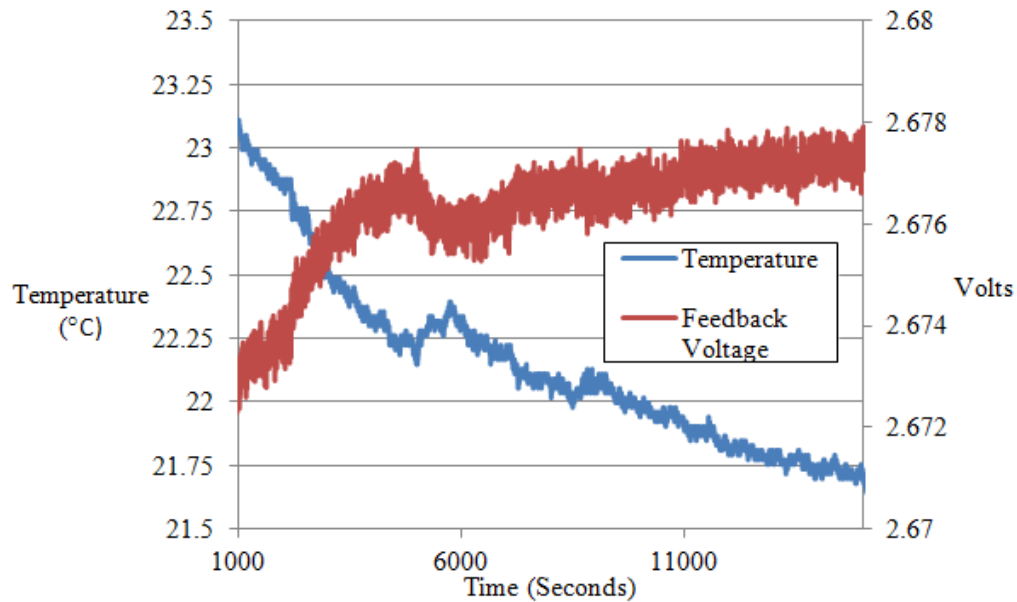
Figure 42: **Relationship between Anemometer Feedback Voltage and Ambient Temperature**

6.3 Fan Control System

The fan in the PMON system was capable of being controlled in several methods. First, it could just be set to the maximum 5 V and run at full speed. Second, a hardware timer could count a number of ticks to occur between back EMF pulses from the fan. A proportional-integral (PI) controller would then correct for any errors between the current fan speed and the desired operating speed. The third method is similar to the second in that it also uses a PI controller. However, this time the controller compared the airflow velocity through the channel with a desired set point and adjusted the PWM accordingly (Figure 43).
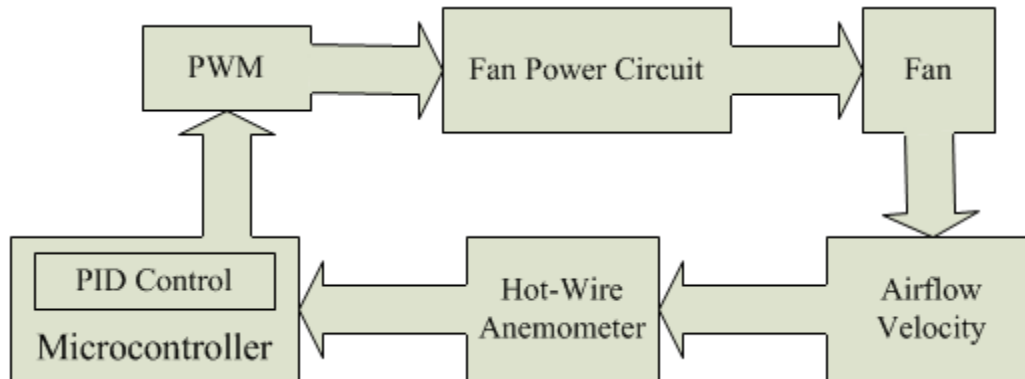
Figure 43: **Alternate Fan Control Loop with Integrated Hot-Wire Anemometer**

The first method, while being the simplest, was not able to produce consistent RPMs between units and led to conflicting results between units during calibration. The second method fixed most of the calibration issues but did not account for the problem for possible variances in the ambient airflow as shown in Figure 11 in Section 3.1.2. Even if good calibration was achieved, the fan's RPM as read by the back EMF pulses could not detect changes in the pressure around the intakes or outtakes. Blockages could occur and alter the airflow velocity but the fan would continue spinning at the same rate.

The third method explored did not employ the back EMF method and instead monitored the actual airflow velocity as measured by the CTA. While the actual fan RPM could still be determined through the back EMF method, its measurements were unnecessary in correcting for errors in the airflow velocity. On the other hand, the relationship between the RPM and the change in the airflow velocity helped to reveal the resolution of control offered by changing the fan speed.

6.3.1 Airflow Velocity and PWM Relationship

Using a calibrated CTA, the PWM high time was incremented slowly while the resulting airflow velocity was recorded. The high time of the PWM signal can be described as the value necessary for achieving the desired duty cycle if the PWM period

is set to 200 counts. The high time can range from 0 to 200, representing a duty cycle of 0 to 100%, respectively. It was found that for every 10 counts high, the airflow velocity was altered by approximately 0.17 m/s (Figure 44).
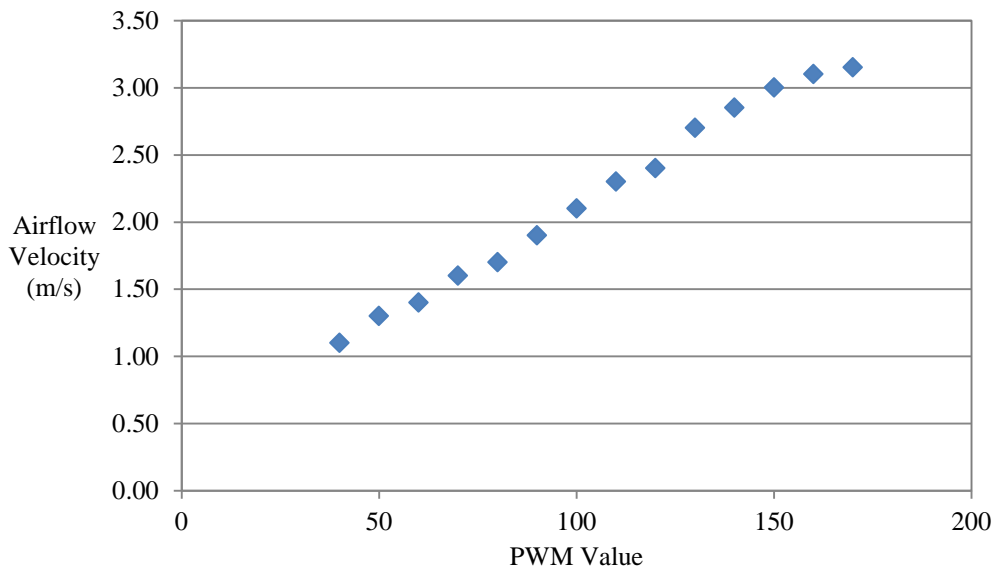
Figure 44:   Airflow Velocity as a Result of PWM Duty Cycle High Time

The minimum PWM value capable of sustaining continuous fan rotation was around 40 counts. It was also found that airflow velocity was unable to increase beyond around 3.1 m/s when the high time was above 160.

6.3.2 Controller Calibration

The effect the PWM value had on the airflow velocity offered a good starting point for determining a proportional gain for the controller. If the anemometer showed an increase of the airflow velocity by 1 m/s, then the immediate change to the PWM value would be a drop of at least 50 counts. In this circumstance, the proportional gain would be approximately 50. However, this approach entails the use of floating point calculations. Given that the control loop for the fan is updated through an interrupt service routine (ISR), the use of floating point should be avoided as much as possible.

The easiest way to prevent the need for floating point is to scale the airflow velocity value by some power of 10 in order to remove the decimal value. The value can then be cast into an integer type for the use within the ISR. For example, if the desired airflow velocity is 3 m/s, and the current airflow velocity is 3.46 m/s, then the error would be -0.46 m/s. Instead of using floating point representation, all values can be scaled by 1000 in order to remove the decimal point. The error then becomes -460, which can then be handled in the form of a signed integer. Scaling the slope of the line shown in Figure 44 by 1000 produces a change of 17 per unit change of the PWM high time. Integer division of -460 by 17 yields a PWM value change of -27. Thus, the proportional gain should be the inverse of 17. Once again, to prevent the use of floating point, the proportional gain will have to be performed as integer division and not scalar multiplication.

Since having a proportional gain set too high would result in an oscillation of the fan, an integral component was necessary. This part of the controller would also assist in making up for airflow lost to external pressure changes or blockages. It is important to note that the integral gain is greatly affected by the sample rate of both the controller and the anemometer. A faster controller sampling speed results in faster accumulation of integral error. If the controller's sample rate exceeds the anemometer's sample rate, integral error will build up and overshoot the target airflow velocity. Once the anemometer has detected the overshoot, the integral will switch directions, resulting in overshoot of the opposite direction. Therefore, it is important that the sampling rate of the anemometer is equal to or faster than the sampling rate of the controller.

In order to assist the ISR even further, integer divisions were replaced with binary bit shifts wherever possible. The proportional gain, being nearly 1/16, could be changed to 4 leftwards bit shifts. The degree of error not covered by the proportional gain could then be handled by the integral error. The integral error was an accumulation of the proportional error. Its gain was also applied through leftwards bit shifts emulating a division by 32.

CHAPTER 7: TESTING AND RESULTS

After validating the anemometer's measurements, an external fan was placed in two positions in relation to the flow channel. The first position was intended to assist the airflow through the channel by pointing the external fan into the intake. The second position had the fan pointed at the outtake in order to hinder the airflow. In both situations, the controller should detect the error of the airflow velocity and attempt to change the internal fan speed.

7.1 Anemometer Verification

To check the accuracy of the calibrated anemometer, its measurements were compared to the EXTECH's measurements. Each probe was inserted into the same test channel in series. Airflow was controlled by varying the fan voltage. Figure 45 contains the results of the measurements for comparison. The test probe and EXTECH are fairly consistent for airflow velocities 4 m/s and greater. The test probe's measurements begin to fall slightly under the EXTECH's measurements for the slower airflow velocities. This may be due to a small inaccuracy in the selection of n during calibration.
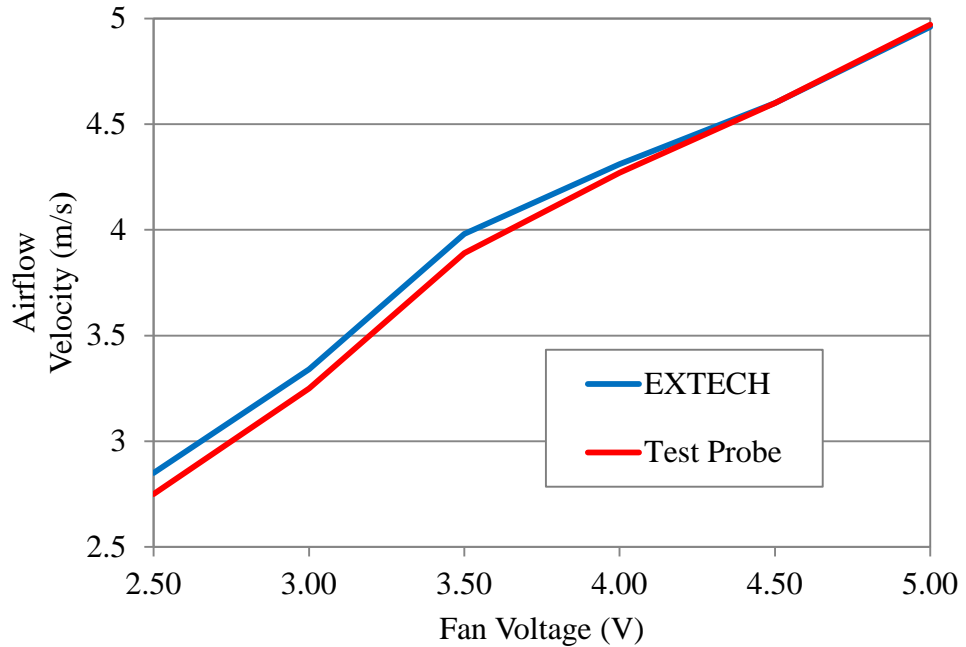
Figure 45: **Comparison of Measurements from Calibrated Test Probe and EXTECH Model**

7.2 Fan Control Results

To ensure that the external fan was in fact assisting the airflow, the fan controller was initially set to static RPM. Figure 46 shows the effect of the disturbance on the airflow while the internal fan was held constant at around 8,000 RPM. As can be seen, the airflow velocity increases noticeably despite the constant rotational velocity of the internal fan.
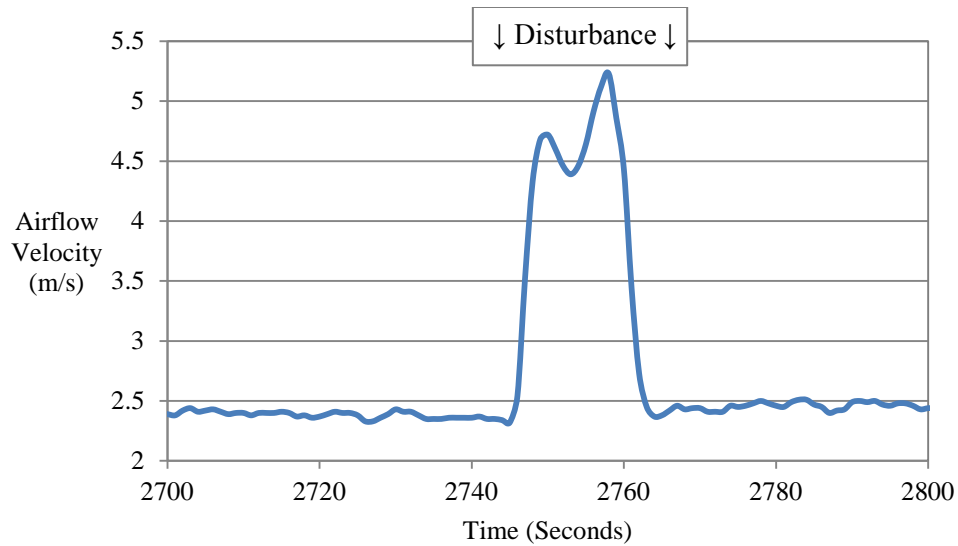
Figure 46: **Effects of External Pressure and Flow Variations on PMON Internal Airflow Velocity**

Enabling the airflow controller at a target velocity of 2 m/s, the same experiment was conducted. Figure 47 shows the airflow velocity of the unit during the test. The controller attempts to maintain the desired 2 m/s but is unable to immediately compensate. The first spike is when the external disturbance source is set to the on position. The system appears to be heavily damped, requiring more than 40 seconds before returning to the proper airflow velocity. The second spike extending below the 2 m/s is when the external airflow velocity is set to the off position. Since the fan is already running slower to compensate for the increased airflow velocity, the immediate airflow through the channel drops significantly. The integrated error that had been accumulated over the previous 40 seconds requires over another 40 seconds before it is removed. The test was then performed again, but with the disturbance hindering the airflow through the channel.
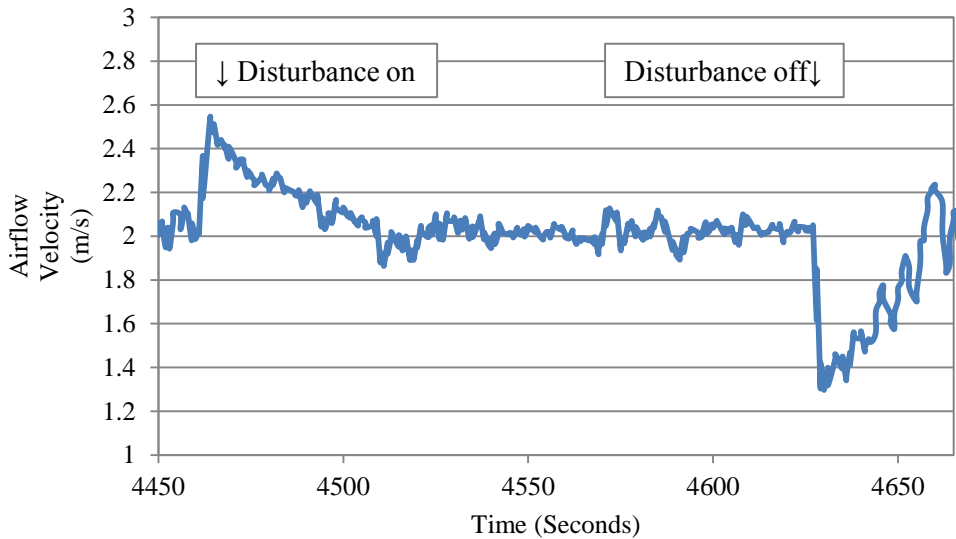
Figure 47: **Airflow Velocity during Assisted Airflow Controller Response**

Figure 48 shows a very similar, although mirrored, result to that of Figure 47. The disturbance provided a loss of airflow velocity seen as the downward spike, which required an acceleration of the fan. The time required to react still proved to be over 40 seconds before the system was resting at a consistent 2 m/s. Once the disturbance ended, the integrated error required a length of time before dissipating, causing the second spike to go above the 2 m/s.
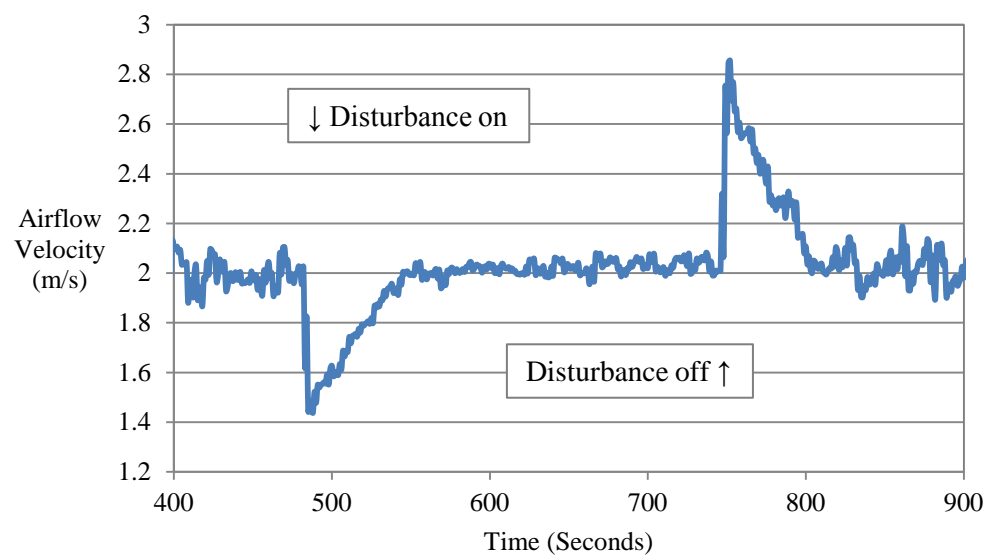
Figure 48: **Airflow Velocity during Conflicted Airflow Controller Response**

The heavy dampening of the system is most likely a result of the low sample rate required by the system. Since the motherboard handles the tasks of many other sensors, the control system was unable to receive the necessary amount of resources that would be required to respond more quickly. As a result, the airflow velocity controller may not be a solution to rapidly changing airflows. However, the system does show the capability of maintaining a desired airflow velocity during a prolonged static disturbance, such as an inlet or outlet blockage.

Another disadvantage of the airflow velocity control system is that the fan is very limited in its ability to compensate for very large disturbances. The average operating airflow velocity range rests between 0 and 4 m/s. If the airflow is hindered by more than 4 m/s, the fan will respond with enough RPM to achieve stability. The inverse also holds true. If the airflow is assisted by an external disturbance large enough, the fan will only be able to shut down. Both scenarios will require another method of compensation to assure accurate PM concentration measurements.

7.3 OPC Compensation Results

The test to verify the OPC compensation method introduced in Section 6.1.3 consisted of placing Unit A and Unit B in the particle chamber. Unit A was again used as a control and experienced no airflow fluctuations in its OPC channel. Unit B contained the hot-wire anemometer and the particle count firmware correction method. An external fan was pointed at the intake of Unit B in order to simulate external air disturbances and to change the airflow velocity internal to Unit B's OPC channel. The particle chamber was evacuated of almost all particulate and then introduced with 0.6 μm PSL. First, the small PM concentration measured by Unit B was evaluated against Unit A's small PM

measurement. Once agreement between the units was confirmed, the airflow through Unit B was increased through the assistance of the external fan.

The airflow velocity through Unit B was stepped down over a period of time while the small PM concentration results were monitored. Figure 49 demonstrates the ability of the compensation to ensure consistent behavior. As is visible, Unit B's PM concentration measurement still tracks Unit A's PM concentration measurement. While the two units do not agree completely, the amount of error previously shown in Figure 27 of Section 6.1.2 has been largely mitigated.
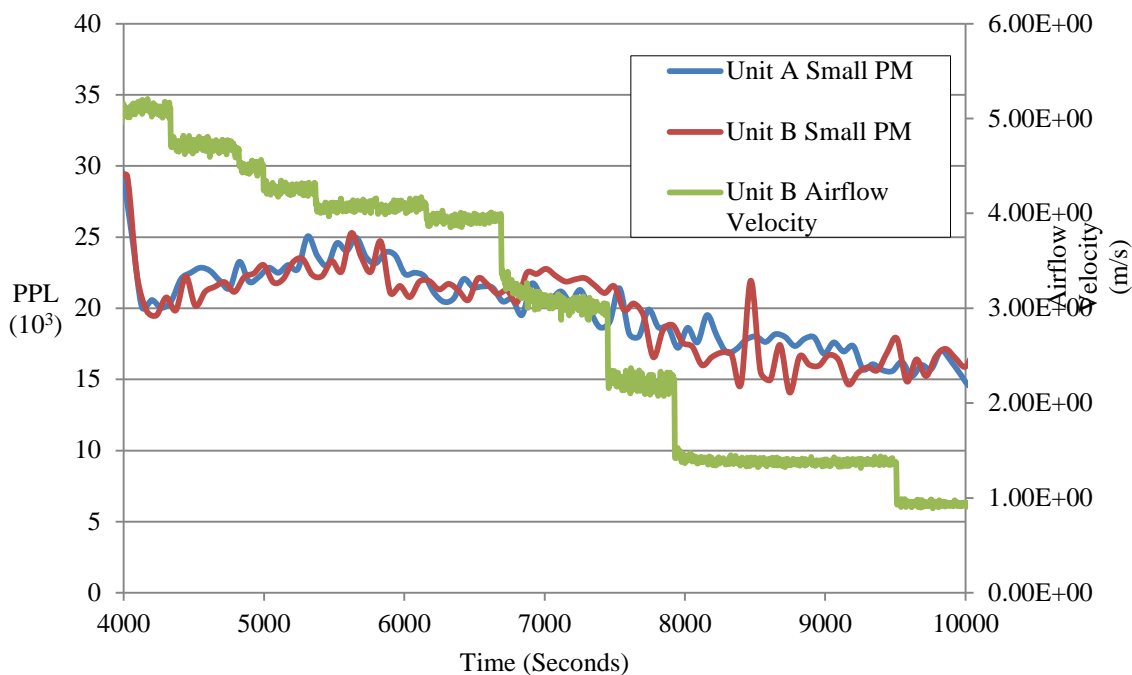
Figure 49: **Comparison between Airflow Velocity and Particle Concentration Measurements after Compensation.**

Not shown in Figure 49 is the effect of an attempt to compensate for an airflow velocity nearing zero. Given that the compensation made to the sample scalar is a ratio between the calibration airflow velocity and the current airflow velocity, the compensation result approaches infinity as the airflow velocity goes to zero.

Consequently, a limit must be kept to ensure that no efforts of compensation are made when the airflow velocity drops below 1 m/s.

Little can be done to fix particulate readings lacking enough airflow. This is due to the fact that PM concentration levels are estimated statistically. Since the volumetric flow rate of the air through the channel acts, essentially, as a sample size, an airflow velocity too low results in the inability to make any empirical inferences about the quality of the ambient air. A PMON unit experiencing such an occurrence should not attempt to compensate for extremely small sample sizes and should, instead, warn the user about the potentially inaccurate measurements.

CHAPTER 8: CONCLUSION AND FUTURE WORK

8.1 Conclusion

The design and integration of a hot-wire anemometer within a flow channel has been discussed and shown to be successful in determining the airflow velocity. A control system on the PMON platform was shown to lack the required resources to operate at a sample rate sufficient for rapid responses. However, it remains a viable solution for prolonged and unchanging disturbances. The OPC compensation method has been shown to maintain consistent measurements for a desired operating range. In the event that external disturbances are numerable and varied, the OPC compensation should be used in lieu of the fan controller to maintain accurate measurements.

In this thesis, a fan-driven OPC has been shown to be improved with the aid of a hot-wire anemometer. The result is a more flexible and stable OPC.

8.2 Future Research

8.2.1 Optical Particle Counter

There are improvements that can be made to the OPC. The most notable problems reside in the maximum RPM of the fan. If a gust forces the flow channel to exceed 5 or 6 m/s, the fan will be unable to compensate. Mechanical alterations to the enclosure may assist with preventing external airflow disturbances, but at a sacrifice of portability. A fan of higher RPM potential should be used if available. However, power cost must still be noted as a more powerful fan will drain the battery faster.

Adding a second photodiode at the laser extinction point may also assist in providing additional features for pattern recognition (see Section 2.2.1). Since a light obscuration OPC can be more sensitive to larger particulate, it can assist in differentiating between larger particles and slowing moving smaller particles. The scattering technique can still be used to assist in detecting finer particulate. The obvious downside is a slight increase in power consumption in the end design and the need for additional space for the physical placement of the second photodiode and its related circuitry.

8.2.2 Hot-Wire Anemometer

Two different configurations have been explored in this research. The CCA was shown to be a viable solution but unnecessarily consumed power and responded slower to temperature variances. The CTA was a direct improvement to the CCA in both efficiency and airflow velocity detection. By incorporating a DAC, the CTA was enhanced with software functionality, assisting in the calibration and control of the anemometer. Consistent and accurate airflow velocity measurements could be obtained upon completion of calibration.

Perhaps an area most requiring improvement would be in the circuit feedback loop of the CTA. The differential amplifier was only capable of delivering a maximum of 80 mA to the probe side of the bridge. This limited the current CTA design to detect air speed velocities of up to 10 m/s. If higher air speeds are present, the amplifier will rail and prevent further data capture. Replacing this amplifier would be a quick solution to prevent this from occurring. However, the tradeoff between anemometer overheating capability and battery life of the system should still be kept in mind when choosing a new amplifier.

While the CVA was briefly discussed in Section 4.4, one had not been designed for this research. This was in part due to the motivations behind the CVA's development. Sarma discusses how the probe capacitance can create varying degrees of noise in the system requiring a reduction to the gain applied to the signal. Longer probe leads created more interference and had to be avoided in the CTA and CCA. However, in the PMON, the probe leads can be kept to a minimal length since both the probe and CTA circuit are contained within the enclosure. The CVA still may yet offer other advantages but will require an investigation in order to determine if some exist.

Another potential improvement to the CTA would be an automated calibration process. As it currently stands, the CTA must used with the test channel where the fan is regulated by a variable power supply. The fitting of the equation to the curve is handled in MS Excel and the results must be placed in the SD card's initialization file. For the sake of convenience, it may be possible to alter the process to remove the human requirement. If known airflow velocities can be sent through the OPC flow channel, the anemometer firmware should be capable of handling the linearization of the voltage versus airflow velocity. Self calibration could then be triggered by placing a file in the SD card prior to system startup.

Decreasing the size of the tungsten wire could also lead to an improvement. While the length of the wire is determined by the width of the PMON flow channel, the thickness could be reduced. A smaller current flow could then be used to achieve higher temperature levels, thus reducing thermal lag and improving sensitivity. However, a thinner wire may also increase the difficulties seen in soldering.

Lastly, the probe creation process required many sensitive steps all performed by hand. The amount of resistance varied from probe to probe causing each to respond differently to the feedback voltage. While the DAC was capable of dealing with this issue for the most part, a more ideal solution would be to mechanize the probe creation process. This would ensure each probe to be as close to the ideal resistance as possible and could prevent damages to the wire from the soldering stage.

8.2.3 Integrated System

The motherboard was a key factor to the development of the multi-sensor system. However, it contained many limitations primarily in the area of processing capability. For example, the fan control code was limited to a single hardware counter/timer module, despite its multi-functionality. Firmware had to be written in a way that shared this timer, often at a price of code efficiency. As a result, fan RPM sensing and control loop update rates had to be lowered. The PMON platform also lacked floating point hardware, which, ultimately, had the most negative effect on the system's software. The anemometer code makes extensive use of floating point calculations in its task loop. While a conscious effort was made to maintain the control loop ISR to be free of floating point code, it was sometimes unavoidable due to the degree of accuracy required for proper functionality.

While some algorithmic solutions may exist to support an integer-based solution, a more viable option exists: move to a processor with floating point hardware. This would reduce the amount of time necessary to process the control loop and sensor task functions, leaving more resources available to other potential sensors. Depending on the processor, other hardware components may also become available.

During the development of the CTA, HSIL had developed a new motherboard containing a processor superior for the PMON. The new motherboard, aliased as the Canary, was designed around an ARM-based (Advanced RISC Machine, Reduced Instruction Set Computer) processor architecture. This processor, the STM32F407ZG, is produced by ST Microelectronics. It provides a faster processing speed, more available hardware options and also includes floating point hardware. Moving the anemometer to the Canary would allow a more abundant use of floating point calculations, thus speeding up sensor tasks.

REFERENCES

[1]   L. Morawska, T. Salthammer, "Indoor Environment: Airborne Particles and Settled Dust" Wiley-VCH, 2003.

[2]   P. M. Haas, United Nations Environment Programme. *Environment*, vol. 36, no. 7, pp. 43, 1994.

[3]   C. Pope, D. Dockery, Health Effects of Fine Particulate Air Pollution: Lines that Connect. *Journal of the Air & Waste Management Association*, vol. 56, no. 6, pp. 709-742, 2006.

[4]   M. Riediker, W. Cascio, T. Griggs, M. Herbst, P. Bromberg, L. Neas, R. Williams, R. Devlin, Particulate Matter Exposure in Cars is Associated with Cardiovascular Effects in Healthy Young Men. *American Journal of Respiratory and Critical Care Medicine*, vol. 169, no. 8, pp. 934-940, 2004.

[5]   G. S. W. Hagler, P. A. Solomon, S. Hunt, "New Technology for Low-Cost, Real-Time Air Monitoring," EM Magazine, August, pp. 6-9, 2014.

[6]   J. Hall, *Seeking Cleaner Air – Accessible Air Quality Monitoring and Event Diagnosis*. Ph. D. dissertation, Boise State University, 2014.

[7]   M. Sajben, "Hot Wire Anemometer in Liquid Mercury," Review of Scientific Instruments, vol. 36, pp. 945, 1965.

[8]   Extech Instruments, "Hot Wire Thermo-Anemometer with Datalogger Model SDL350 User Guide" [Online]. Available: http://www.extech.com/instruments/resources/manuals/sdl350_um.pdf/.

[9]   United States Environmental Protection Agency, "Federal Register Part II 40 CFR Part 50, National Ambient Air Quality Standards for Particulate Matter," vol. 71, no. 200, pp. 61144–61233, 2006.

[10]   D. Soldo, A. Quarto, "M-DUST: an Innovative Low-Cost Smart PM Sensor," Instrumentation and Measurement Technology Conference (I2MTC), 2012 IEEE International, pp. 1823-1828, May 2012.

[11]   A. Sabin, "An Overview of Micron-Ranged Particle-Sizing Techniques," Journal of GXP Compliance, vol. 16, no. 1, pp. 57-65, 2012.

[12]   H. Zhang, C. H. Chon, X. Pan, D. Li, "Methods for counting particles in microfluidic applications," Microfluidics and Nanofluidics, vol. 76, pp. 739-749, 2009.

[13]   L. H. Schmoll, T. M. Peters, P. T. O'Shaughnessy, "Use of a Condensation Particle Counter and an Optical Particle Counter to Assess the Number Concentration of Engineered Nanoparticles," Journal of Occupational and Environmental Hygiene, vol. 7, no. 9, pp. 535-545, 2010.

[14]   Dylos Corporation, "DC1100 Air Quality Monitor." [Online]. Available: http://www.dylosproducts.com/ornodcairqum.html. [Accessed:1-Sep-2014].

[15]   P. C. Stainback, K. A. Nagabushana, "Review of Hot-Wire Anemometry Techniques and the Range of their Applicability for Various Flows," Electronic Journal of Fluids Engineering, Transactions of the ASME, 1996. Web, 17 July, 2014.

[16]   W. K. George, P. D. Beuther, A. Shabbir, "Polynomial Calibrations for Hot Wires in Thermally Varying Flows," Experimental Thermal and Fluid Science, vol. 2, pp. 230-235, 1989. Web, July, 2014.

[17]   G. R,. Sarma, "Analysis of a constant voltage anemometer circuit," *Instrumentation and Measurement Technology Conference, 1993. IMTC/93. Conference Record. , IEEE* , vol. 731, no. 736, pp. 18-20, May 1993. Web, July 2014.

[18]   C. Huang, *Micromachined sensors and actuators for fluids mechanics research and high-speed flow control applications*. Ph. D. dissertation, University of Michigan, 1998.

[19]   A. Pollard, M. Uddin, A.-M Shineeb, C. G. Ball, "Recent advances and key challenges in investigations of the flow inside human oro-pharyngeal-laryngeal airway" International Journal of Computation Fluid Dynamics, vol. 26, no. 6-8, pp. 363-381, 2012.

[20]   D. F. Elger, *An Experimental and Analytical Study of the Internal Fluid Dynamics of an Ink-Jet Printhead (Orifice, Resonator, Impedance, Oscillating, Anemometer)*. Ph. D. dissertation, Oregon State University, 1986.

[21]   H. Siebert, K. Lehmann, R. A. Shaw, "On the Use of Hot-Wire Anemometers for Turbulence Measurements in Clouds," Journal of Atmospheric and Oceanic Technology, vol. 24, no. 6, pp. 980-983, 2007.

[22]   L. Bennett, "Insect Aerodynamics: Vertical Sustaining Force in Near-Hovering Flight," Science, vol. 152, no. 3726, pp. 1263-1266, 1966.

[23]   B. H. Nall, "Use of a hot wire anemometer as a particle velocity detector in standing sound waves," Review of Scientific Instruments, vol. 48, pp. 499, October 1976. Web, July 2014

[24]   S. Corrsin, "Extended Applications of the Hot-Wire Anemometer," Review of Scientific Instruments. vol. 18, pp. 469, March 1947. Web, July 2014.

[25]   R. P. Clark, "A Particle Detector for Use in Ventilation Engineering" The Journal of Hygiene, vol. 71, no. 3, pp. 577-583, 1973.

[26]   C. L. Roozeboom, M. A. Hopcroft, W. S. Smith, J. Y. Sim, D. A. Wickeraad, P. G. Hartwell, B. L. Pruitt, "Integrated Multifunctional Environmental Sensors" Journal of Microelectromechanical Systems, vol. 22, no. 3, pp. 779-793, 2013.

[27]   Particle Measuring Systems, "PMS Lasair II 110 Datasheet." [Online]. Available: http://www.pmeasuring.com/particleCounter/air/mobile/L2110.

[28]   TSI Incorporated, "TSI Aerotrak 9303 Datasheet." [Online]. Available: http://www.tsi.com/aerotrak-handheld-particle-counter-9303/.

[29]   T. L. Bergman, A. S. Lavine, F. P. Incropera, D. P. Dewitt, "Fundamentals of Heat and Mass Transfer, Seventh Edition," John Wiley & Sons, 2011.

[30]   H. Kramers, "Heat Transfer from Spheres to Flowing Media," Physica, vol. 12, pp. 61-120, 1946. Web, July, 2014.

[31]   P. Ligęza, "Constant-Bandwidth Constant-Temperature Hot-Wire Anemometer," Review of Scientific Instruments. vol. 78, July 2007. Web, July 2014.

[32]   G. Comte-Bellot, J. Weiss, J.C. Béra, "Lead-resistance effects in a constant voltage anemometer," Review of Scientific Instruments, vol. 75, pp. 2075, 2004. Web, July 2014.

[33]   Z. Yue, T. Malmström, "A simple method for low-speed hot-wire anemometer calibration," Measurement Science and Technology, vol. 9, pp. 1506-1510, 1998.

[34]   P. Ligęza, "On unique parameters and unified formal form of hot-wire anemometric sensor model," Review of Scientific Instruments, vol. 76 pp. 126105, 2005.